

**INVESTIGATIONS OF QCD  
HADRONIZATION USING JETS  
MEASURED AT  $\sqrt{s} = 8$  TeV WITH  
THE ALICE DETECTOR.**

A Dissertation Presented for the

Doctor of Philosophy

Degree

The University of Tennessee, Knoxville

Andrew John Castro

March 2019

© by Andrew John Castro, 2019

All Rights Reserved.

# Chapter 1

## Introduction

From the Vedas to the ancient Greeks, generations have described the constituents of nature in terms of indivisible ‘elements’. It wasn’t until the beginning of the 20th century that the ancient elements of earth, wind, fire, water, and the aether were abandoned for the atomic theory of nature. By the 1960’s, what would become known as the Standard Model of Particle Physics was taking shape. The five ancient elements were replaced by the fundamental particles: quarks and leptons comprising the spin 1/2 fermions and the force carrying bosons with spin 1 as seen in Fig. 1.1

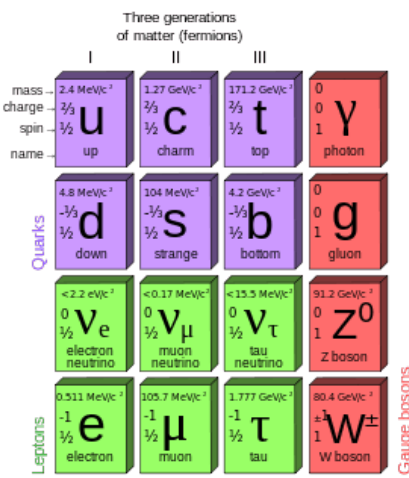


**Figure 1.1:** The fundamental particles of the Standard Model[? ].

The Standard Model is the unification of the three symmetry groups,  $SU(3) \times SU(2) \times U(1)$ , representing the strong, weak, and electromagnetic forces[? ]. In terms of scientific

accomplishments the Standard Model is one of the most tested theories of nature with an agreement between the theory and observed results up to ten digits[? ].

Even though the Standard Model gives us a deep understanding for many natural phenomena and has a wide range of uses; understanding the evolution of the Big Bang, how atoms and molecules bond, the nature of light, to cancer treatments and nuclear security it is fundamentally an incomplete theory of nature. The fact that Gravity has yet to be unified into a quantum theory tells us that the Standard Model is incomplete. High energy experiments give us some of the most extreme conditions possible to test the Standard Model and to look for phenomena outside of the theory. Are their new symmetries and laws that manifest at high energies? Can we create dark matter or dark energy in a laboratory? Are quarks and leptons fundamental or finite in size? Do the four fundamental forces emerge from some yet unknown unified force? And why is antimatter absent in the Universe? All of these open questions are of great interest and currently form large areas of active research.

The theory of strong interactions, Quantum Chromodynamics(QCD), is described by the SU(3) group and similar in analogy to the electric charge of Quantum Electrodynamics (QED) carries color charge, red, green, and blue. Quarks and gluons are colloquially known as partons and are particles that interact via the strong force. At low energies and over large length scales partons are confined to a color neutral state and these particles must clump together into color neutral hadrons. As two colored partons began to separate, at some point it becomes energetically favorable to create a quark–antiquark pair out of the vacuum rather than expanding the distance between neighboring partons. Due to confinement, quark interactions at high energy collider experiments manifest themselves as a spray of hadrons known as a ‘jet’. The other main attribute of QCD is asymptotic freedom, as the interactions between partons becomes more energetic and the length scale decreases the strong coupling constant becomes exceedingly small,  $\alpha_{strong} \ll 1$ , and the partons freely interact with one another. Due to asymptotic freedom nuclear matter undergoes a phase transition called the Quark–Gluon Plasma (QGP) at high energies and densities

This thesis will present an overview of Quantum Chromodynamics in Chapter 2, with an emphasis on jet physics and heavy ion collisions. Chapter 3 will give a brief overview of the Large Hadron Collider and the ALICE experiment, including the relevant subsystems

for this jet analysis. Jet results from the ALICE detector along with comparissons to QCD simulations with systematic uncertainty calculations and unfolding for detector effects will be given in Chapter 4. The ALICE time projection chamber will be upgraded to a continous readout mode, the physics motivation behind this and author's contributions will be discussed in Chapter 5. Chapter 6 will serve as a final discussion, outlook, and conclusion.

# Chapter 2

## Quantum Chromodynamics

In 1968 deep inelastic scatterings performed at the Stanford Linear Accelerator Center showed that the proton had internal structure[1] called partons at the time. Within a decade of this discovery the partons were broken into two categories: the mass carrying fermions were known as the quarks and the gauge boson force carriers were called gluons. The interactions of these two types of particles were described by the quantum field theory known as Quantum Chromodynamics (QCD) and by the SU(3) symmetry group. SU(3) guarantees that color charge is conserved and this results in quarks grouping together into ‘colorless’ hadrons.

### 2.1 The QCD Lagrangian

QCD is the strongest of the known fundamental forces. It is a gauge field theory described by the Lagrangian density

$$\mathcal{L} = -\frac{1}{4}F_{\mu\nu}^\alpha F_\alpha^{\mu\nu} - \alpha_s(\bar{q}_j \gamma^\mu T_\alpha q_j)G_\alpha^\mu + \bar{q}_j(i\gamma^\mu \partial_\mu - m)q_j \quad (2.1)$$

where  $q$  and  $\bar{q}$  represent the color anti-color fields summed over color  $j$ ,  $\alpha_s$  is the strong coupling strength,  $\gamma^\mu$  is the Dirac gamma matrix,  $G_\alpha^\mu$  is the gauge field for color  $\alpha$ , is similar in analogy to the  $\mathbf{W}$  matrix from the electroweak theory.  $F_{\mu\nu}^\alpha$  is the field strength tensor and it describes the gluon interactions. The first term of the Lagrangian is the gluon contribution

and carries no mass term. The second term of the Lagrangian describes how quarks and gluons interact with each other. The final term describes quark interactions and the coupling between them and will be explored further in this thesis.

At short distances, less than  $0.2 \text{ fm}$ , the strong coupling constant becomes exceedingly small and second term of the Lagrangian displays an important property known as asymptotic freedom[2].

$$\alpha_s = \frac{1}{\beta_0 \ln(Q^2/\Lambda^2)} \quad (2.2)$$

where  $\alpha_s$  is the strong coupling constant,  $Q^2$  is the momentum transfer between two interacting partons, and  $\Lambda^2$  is a cutoff below which QCD phenomena are strongly suppressed and  $\beta_0$  is a correction factor.

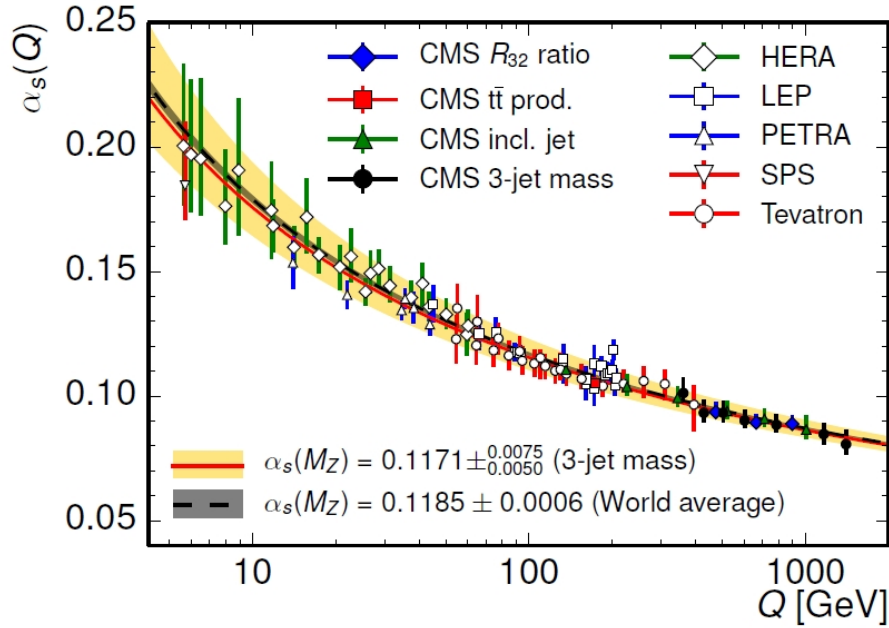


**Figure 2.1:** Strong coupling constant ( $\alpha_s$ ) as a function of the momentum transfer ( $Q$ )[3].

## 2.2 Jets

Hard probes (large  $Q^2$  interactions), are produced in the earliest stages of a high energy collision when the largest momentum transfer processes occur. As two highly energetic

partons propagate away from one another, in a back-to-back fashion, they will instigate a shower of daughter partons via gluon radiation and the generation of low-mass  $q\bar{q}$  pairs. These daughter partons will go on to form hadrons and the clustering of these hadrons is colloquially known as a ‘jet’. If the jet was created in a high energy experiment the final state hadrons will be recorded as tracks in a tracking detector or energy deposits in a calorimeter. This process is shown in Figure 2.2.

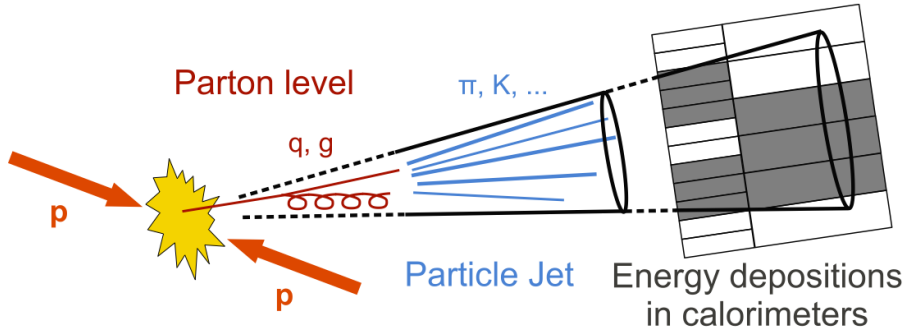


**Figure 2.2:** Diagram showing a jet created by two partons under going a hard scattering, forming into hadrons, and detected in a calorimeter[4].

The physicist James Daniel Bjorken postulated that a correlation could be surmised by summing over the final state transverse momentum of the hadrons that form a jet to the parton that initiated the hard scattering[5][6]. This has lead to jets becoming the work-horse for both experimentalists and theorists over the past 30 years in probing QCD phenomena. This thesis makes use of jets as an important probe of QCD and the following sections are devoted to developing a background for both the theoretical and experimental treatment of jet physics. The following sections will be devoted to how jets are produced from a physics point-of-view and the latest results which this thesis compares to.

### 2.2.1 Jet Production and the Factorization Theorem

Due to confinement bare quarks are unobserved, therefore experimentalists must probe QCD interactions by detecting the color neutral final state hadrons measured in collider experiments. Fortunately, the factorization theorem (Equation 2.3) allows for the final state jet cross section to be broken into a number of steps that can either be calculated

perturbatively using pQCD or modeled phenomenologically. Using the factorization theorem the jet cross section in a pp collision is,

$$d\sigma^{pp \rightarrow jet} \sim f_{a/A}(x_1, Q^2) \otimes f_{b/B}(x_2, Q^2) \otimes d\sigma_{ab \rightarrow c+X}(x_1, x_2) \otimes D_{c \rightarrow h/jet}(z, Q^2) \quad (2.3)$$

- $f_{a/A}(x_1, Q^2)$  and  $f_{b/B}(x_2, Q^2)$  are the parton distribution functions (PDF) that describe the probability of finding parton,  $a$  or  $b$ , within nuclei,  $A$  and  $B$ , with a given momentum fraction,  $x = p_{parton}/p_{hadron}$  as a function of  $Q^2$ .
- $d\sigma_{ab \rightarrow c+X}(x_1, x_2)$  is the pQCD parton-parton cross section due to the hard scattering of the two partons,  $a$  and  $b$ , to an intermediate parton ( $c$ ).
- $D_{c \rightarrow h/jet}(z, Q^2)$  is the fragmentation function (FF) that describes the probability the an outgoing parton,  $c$ , fragments and hadronizes into a final state hadron,  $h$ , within a jet with momentum fraction,  $z \equiv p_{hadron}/p_{parton}$ .

Figure 2.3 shows a timeline of a pp collision broken into the relevant steps in accordance to the factorization theorem. One of the best places to fundamentally test QCD phenomena using hard probes, i.e. jets, are with high energy hadron colliders such as those found at CERN<sup>1</sup>, Fermilab, and BNL. The time scale that a hard probe is created in a high energy collision is on the order of  $\tau \approx 1/p_T \approx 0.1 \text{ fm}/c$  which probes the initial state these interactions. The factorization theorem allows for a high level of agreement between the QCD theory of nature and experimental observables but to ascertain this connection we should discuss each term of the factorization theorem in more depth.

## Parton Distribution Functions

The PDF occurs twice in Equation 2.3 due to the two partons that will undergo the hard scattering being confined in two different protons. PDFs may be thought of as conveying the structure of a nucleon in terms of the number of flavored quarks or gluons ( $u(x)$ ,  $d(x)$ ,

---

<sup>1</sup>Discussed in detail in Chapter 3

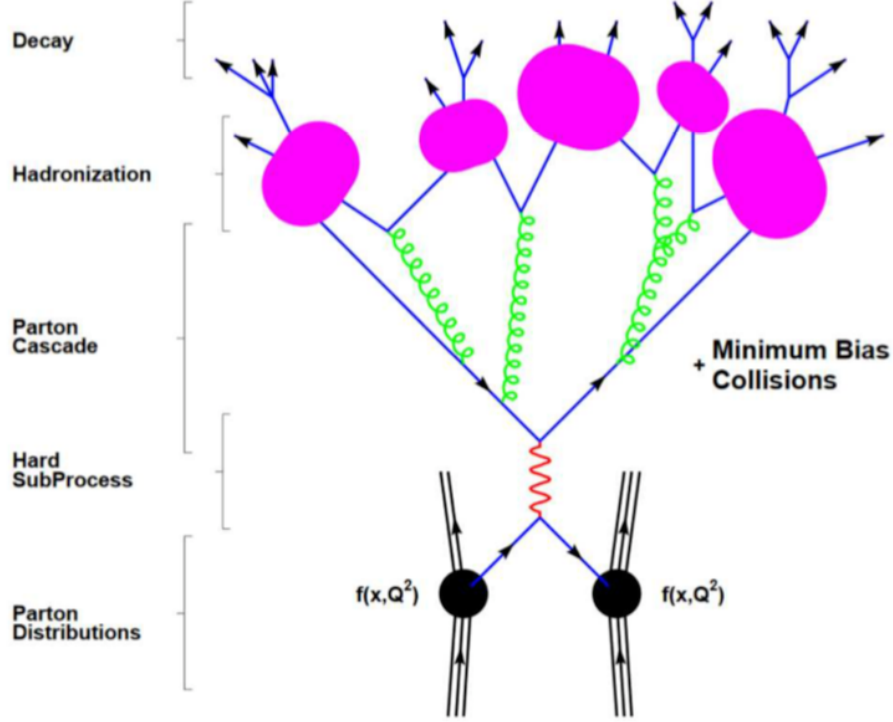


**Figure 2.3:** Timeline of a proton-proton collision. Starting from the bottom, two partons confined within the colliding protons have a hard interaction. The outgoing partons will induce partonic showers by radiating quarks and gluons. The partonic showers will eventually form into final state hadrons due to confinement which are measured in high energy experiments[7].

$s(x), \bar{u}(x), \bar{d}(x), \bar{s}(x), g(x)$ ) and must obey certain constraints and summation rules. In the case of a proton, with electric charge ( $e = +1$ ),

$$+1 = \frac{2}{3} \int_0^1 [u(x) - \bar{u}(x)] dx - \frac{1}{3} \int_0^1 [d(x) - \bar{d}(x)] dx \quad (2.4)$$

and isospin ( $I = 1/2$ ),

$$\frac{1}{2} = \frac{1}{2} \int_0^1 [u(x) - \bar{u}(x)] dx - \frac{1}{2} \int_0^1 [d(x) - \bar{d}(x)] dx \quad (2.5)$$

have a solution,

$$\int_0^1 [u(x) - \bar{u}(x)] = 2 \quad (2.6)$$

$$\int_0^1 [d(x) - \bar{d}(x)] dx = 1 \quad (2.7)$$

This corresponds to the classical partonic view that protons contained two up quarks and a down quark, similarly the neutron, with charge  $e = 0$  and isospin  $I = -1/2$ , can be shown that it compromises two down quarks and a up quark. Naively, we could assume that the three quarks composing a proton would each carry a momentum fraction of approximately  $1/3$  the total momentum of a proton. However, high energy deep inelastic scattering experiments conducted at the Stanford Linear Collider in the 1960's[8] measured the momentum carried by the three quarks only accounting for about  $1/2$  the total proton momentum. This lead to a more complex and dynamic model of the proton structure with the other half of the proton momentum being occupied by neutral partons which would eventually become known as gluons.

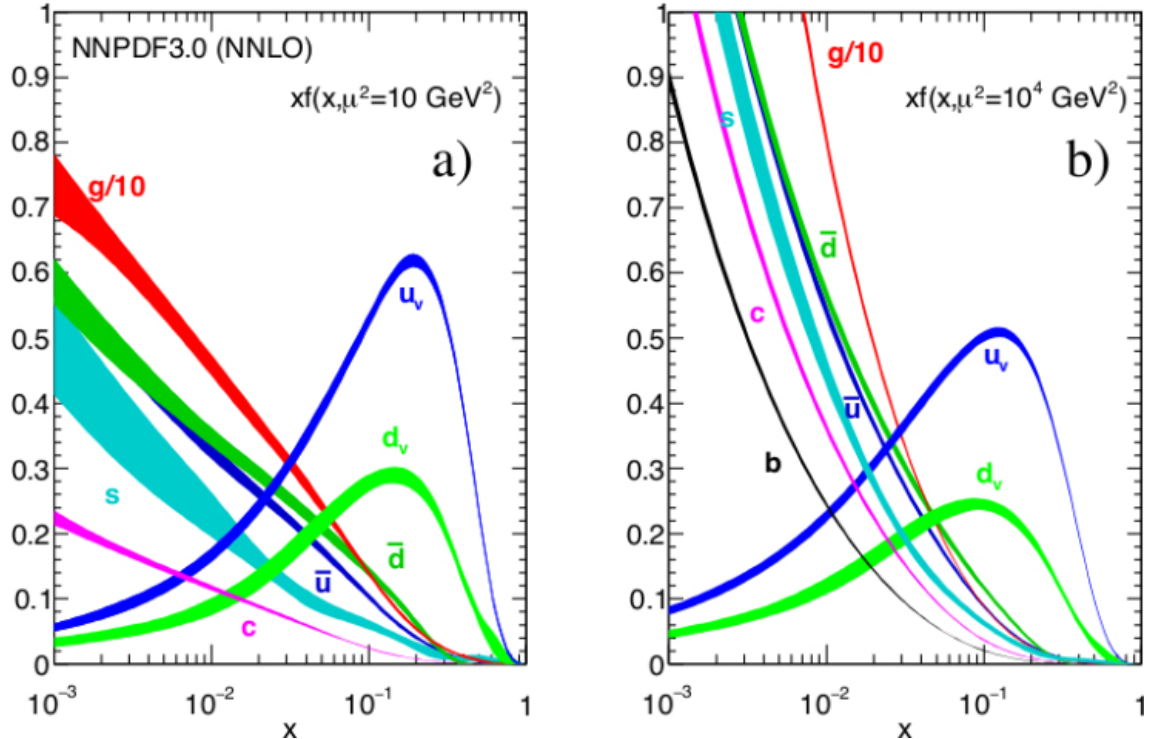


**Figure 2.4:** Proton PDF at  $Q^2 = 10 \text{ GeV}$  (left) and  $Q^2 = 10 \text{ TeV}$  (right) from the NNPDF Collaboration[9].

Measuring the structure of the partons making up a nucleon is a major endeavor by both theorists and experimentalists. Two of the most popular PDFs available to physicists are the CTEQ[10] (Coordinated Theoretical-Experimental Project on QCD) and the NNPDF[11] (Neural Network Parton Distribution Function) sets. Figure 2.4 shows the proton PDF as

a function of the momentum fraction for two energy ranges, at high values of  $x$  the two up quarks account for about 2/3 of the momentum fraction while down quark accounts for about 1/3 the total momentum, these quarks are collectively called the valence quarks. At high energies, low values of  $x$ , we see that the proton has non negligible contributions from gluons, anti-quarks, strange, and even charm quarks, these are collectively known as the sea partons. Today, the modern picture of a protons structure is that it is mostly composed of gluons and sea quarks at low values of  $x$  and this domination only increases as a function of  $Q^2$ [12].

### Parton-Parton Cross-Section

The parton-parton cross section can be calculated using perturbation theory. To the zeroth order in  $\alpha_s$  this cross-section would be a simple quark-antiquark annihilation and would be calculable using Feynman diagrams as seen in Figure 2.5[13]. Higher ordered contributions, such as the creation of virtual gluons, require the hard cross-section to be expanded as a series in terms of  $\alpha_s$ . Calculations of the hard cross section that incorporate these higher order terms are known as *next-to-leading order* (NLO) with  $N$  denoting the number of terms after the leading order that have been included in the cross-section calculation. Various calculations of the hard cross-section of different QCD processes have been performed over the years typically using either power series or logarithmic expansions of  $\alpha_s$ [14] and corrections for LO, NLO, and even NNLO constitutes a very active field in high energy physics.

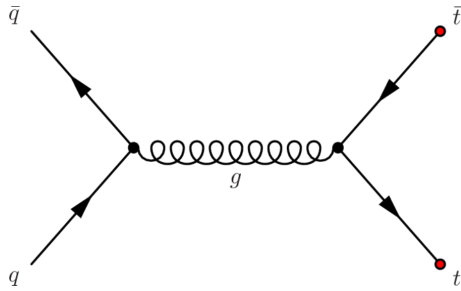


**Figure 2.5:** Lowest order quark-antiquark annihilation to top-antitop pair[15].

Perturbative techniques of the hard cross-section have been extremely successfully in describing jet features in hadronic collisions[12].

## Hadronization

Hadronization is the process by which the colored pQCD partons of form into colorless non-pQCD hadrons and represents a significant barrier in progressing jet physics. This is due to the fact that hadronization encompass several smaller processes which in themselves are hard to characterize. Thus, like PDFs, an accurate description of hadronization requires a phenomenological approach by which experimental results help complement theoretical calculations. Jet production via hadronization[16] follows two distinct stages. First, the partons that underwent a hard scattering start to emit radiation via gluon bremsstrahlung up until time,  $t < Q^2$ , this is known as the parton cascade. The parton cascade is the precursor of what will become a jet as most of the radiation generated will travel in the same direction as the initial hard scattered parton. However, this immediately poses an issue in jet physics as radiation generated at a wide angle away from the momentum axis of the initial hard scattered parton will not be associated with the jet.

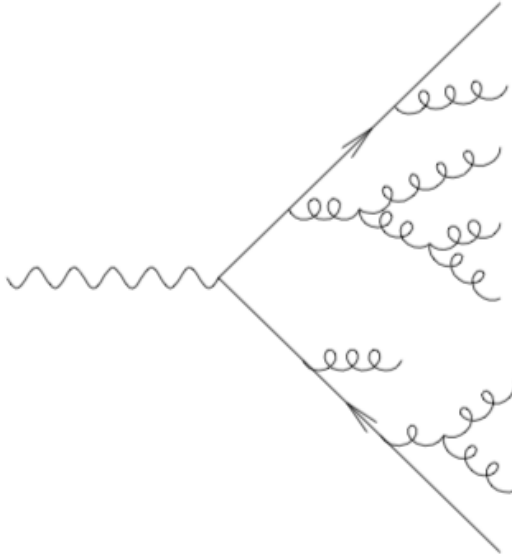


**Figure 2.6:** Parton cascade in a hadronic collision[16].

After the cascade has ended the partons must fragment into color neutral hadrons. There are two main phenomenological models used to describe the hadron forming process, the Lund String Model and the Cluster Hadronization Model. The QCD potential is,

$$V(r) = -\frac{\alpha_s}{r} + \sigma r \quad (2.8)$$

where the first term of Equation 2.8 goes as the Coulomb potential with a  $1/r$  dependence and is the dominate term at short distance and the second term has a string-like potential with  $\sigma$  referring to a string-like tension. The Lund String Model ignores gluon radiation and has fragmentation occur via breaking the string tension with the production of  $q\bar{q}$  sea quarks. The created sea quarks will carry some momentum fraction,  $z$ , of the initial parton until  $z$  falls below some cutoff. Figure 2.7 shows a two quarks undergoing a string breaking, each of the quarks initiating the string breaking will combine with a sea quark in an iterative manner to form hadrons.

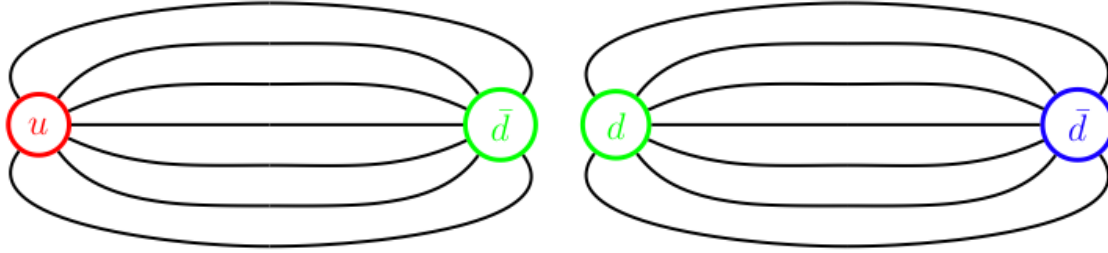


**Figure 2.7:**  $u\bar{d}$  generating a  $d\bar{d}$  pair via string breaking which will form color neutral hadrons, black lines show the string like equipotentials.[17].

The Cluster Hadronization Model has gluons splitting after the parton cascade phase into  $q\bar{q}$  pairs. These pairs will form color-singlet clusters with other neighboring quarks in phase-space. These color-singlets will typically be a few  $\text{GeV}/c^2$  in mass and are treated as excited meson resonances. These psuedo-resonances will decay via their normal branching ratios into the stable hadrons[18].

## Fragmentation

Similar to how a PDF quantitatively describes the structure of a nucleon the FF quantitatively describes the hadronization process. The FF is also similar to the PDF in that it is also a probability distribution, thus it follows the probabilistic rule that,

$$\sum \int z D_{c \rightarrow h/jet}(z, Q^2) dz = 1 \quad (2.9)$$

Ideally, the fractional momentum of the hadrons created from the fragmenting parton,  $z \equiv p_{\text{hadron}}/p_{\text{parton}}$ . Due to the confinement of partons we must use a suitable substitution for measuring the FF. The Parton-Hadron Duality[19] states that a hadron found near the center of a jet should encompass the quantum numbers and kinematic properties associated with the hard scattered quark that initiated the jet. Thus we can measure the fragmentation function as  $z = p_{\text{hadron}}/p_{\text{jet}}$ . The formulation of the FF as a fractional energy carried by the hadrons in a jet was a breakthrough in pQCD techniques and is analogous to how an electron passing through an absorber creates photon showers with these photons generating conversion electrons until the total energy has been dissipated into the material.

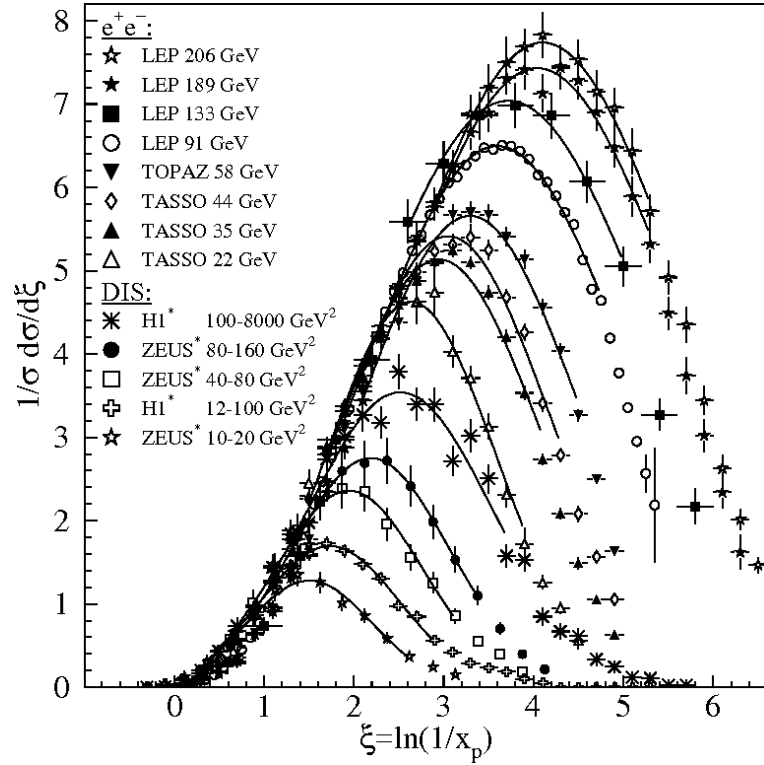


**Figure 2.8:** Fragmentation Functions from  $e^+e^-$  and DIS experiments with fits[20].

Figure 2.8 is the FF in terms of the Gaussian equation,  $z dN/dz = -dN/d\xi$  with  $\xi = -\ln 1/z$ . The observation that the Gaussian peaks of Figure 2.8 along with the suppression of the FF at low  $z$  values due to gluon coherence were predicted by pQCD.

## 2.3 Jet Finding Algorithms

A jet arises from the fragmentation of a hard parton to final state hadrons. However, grouping the hadrons together into a jet is a non-trivial task and jet finding algorithms are deployed in order to achieve this objective. Early on in jet physics, both theorists and experimentalists used a wide variety of jet finders that made comparisons between experiments or to theoretical calculations nearly impossible[21]. For example, a radiated gluon that splits into a quark anti-quark pair may become one or two jets depending on the angular separation and the algorithm used. Early jet finders tended to be sensitive to soft particles or could give widely varying yields to the number of jets in an event. In 1990, the Snowmass Accord[22] was held in order to standardize the definition of a jet between experimentalists and theorists. The agreement maintained that any algorithm that clusters particles into a jet must be both infrared and collinear safe (IRC).

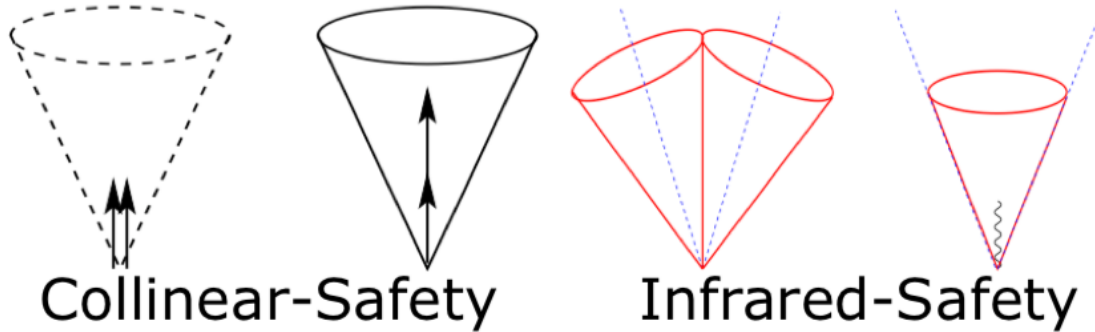


**Figure 2.9:** Cartoon showing Collinear and Infrared safe jet candidates[23].

Collinear safety ensures that a high- $p_T$  particle split into two or more particles should not influence the kinematics of a hard jet, this makes the jet finders insensitive to how hadrons are grouped together. Infrared safety in turn requires that the emission of soft radiation should not affect the properties of a jet, this makes jets returned by the algorithm independent of soft physics and a true signature of a hard process. Both of these processes are shown in Figure 2.9. After the adoption of these standards from the Snowmass Accord, old algorithms that violated these rules were patched and new jet finders were developed to comply with IRC safety. The most prevalent jet finding algorithms today fall into two categories: cone algorithms and sequential recombination/clustering algorithms.

### 2.3.1 Cone Algorithms

Cone algorithms made up the bulk of early jet finders. The only IRC safe cone algorithm still in use today is the seedless infra-red safe cone algorithm (SIScone). SIScone defines a cone of radius, R, around the highest momentum particle in the coordinates of  $(\eta, \phi)$ <sup>2</sup>, this is the proto-jet. SIScone then proceeds through an iterative process of finding all the particles within the jet radius such that  $R \leq \sqrt{\phi^2 + \eta^2}$  and calculates a new jet center based on these particles momenta and a new weighted jet axis  $(\eta, \phi)$ . If the new center matches the proto-jet center, the proto-jet is tagged as a stable jet, all the particles in that jet are removed, and SIScone moves onto the next highest  $p_T$  particle. Cone algorithms tend to be unpopular due to being computationally expensive, they are hard to implement theoretically, and can give results not calculable in perturbation theory.

### 2.3.2 Sequential/Recombination Algorithms

The other class of jet finders are the sequential/recombination algorithms, which are favored by experimentalists, theoreticians and are IRC safe. There are three types of sequential/recombination algorithms:  $k_T$ , Anti- $k_T$ , and the Cambridge/Aachen jet finders, with  $k_T$  referring to the transverse momentum of particle. All of the algorithms use a similar method, first they find the distance between every pair of particles,  $d_{i,j}$ , such that

$$d_{i,j} = \min[p_{T,i}^a, p_{T,j}^a] \frac{\Delta_{ij}^2}{R^2} \quad (2.10)$$

where  $p_{T,i}^a$  is the transverse momentum of particle  $i$ ,  $a$  is free parameter that is set based on which algorithm is used,  $\Delta_{ij}^2 = (\eta_i - \eta_j)^2 + (\phi_i + \phi_j)^2$  is the distance between the particles, and  $R$  is the radius of the jet. A second distance is defined in the sequential/recombination algorithm scheme,

---

<sup>2</sup>It is possible to use a Cartesian coordinate system in particle colliders, with the z-component referring to points along the beam axis while the xy-plane is perpendicular to the beam axis. However, this system is not invariant under a Lorentz boost. Therefore it is more useful to use the cylindrical-like coordinates of pseudorapidity ( $\eta$ ) and the azimuthal angle ( $\phi$ ). Pseudorapidity may be thought of as the polar angle in a cylindrical coordinate system with  $\eta = 0$  when the polar angle is perpendicular to the beam axis and  $\eta = \infty$  along the beam axis.  $\phi$  is the azimuthal angle that rotates around the beam axis. Both,  $\eta$  and  $\phi$  are invariant for Lorentz boosts along the beamline and allow for easy comparisons between the center-of-mass frame and the laboratory frame of a high energy collision.

$$d_{i,B} = p_{T,i}^a \quad (2.11)$$

this is the distance between a given particle  $i$  and the beam axis. Sequential/Recombination algorithms find the set of all particles,  $d_{i,j}, d_{i,B}$ , such that if  $d_{i,B}$  is the minimum for particle  $i$  it is tagged as a jet and removed from the list. If  $d_{i,j}$  are a minimum for particles  $i$  and  $j$  these two particles are merged together into a new particle  $(ij)$  and a new minimum is found between  $(ij)$  and particle  $k$  until all the particles are either merged into jets or the minimization function is no longer satisfied.

### $k_T$ Algorithm

The  $k_T$  algorithm sets the value  $a$  to 2, this results in a minimization function,

$$d_{i,j} = \min[p_{T,i}^2, p_{T,j}^2] \frac{\Delta_{ij}^2}{R^2} \quad (2.12)$$

which clusters low momentum particles first, making this algorithm susceptible to the underlying event (UE) or pile-up (PU). Thus the  $k_T$  algorithm is good at estimating any background present in a high energy collision.

### Anti- $k_T$ Algorithm

The Anti- $k_T$  algorithm sets the value  $a$  to -2, resulting in a minimization function,

$$d_{i,j} = \min\left[\frac{1}{p_{T,i}^2}, \frac{1}{p_{T,j}^2}\right] \frac{\Delta_{ij}^2}{R^2}. \quad (2.13)$$

The minimization function is dominated by high- $p_T$  particles, thus the area and axis of a jet is only slightly perturbed by soft particles. This makes the Anti- $k_T$  algorithm robust in jet finding with events having a UE and PU. The Anti- $k_T$  algorithm is the default jet finding algorithm used at the Large Hadron Collider and is the one used in this thesis.

### Cambridge/Aachen Algorithm

The Cambridge/Aachen algorithm sets  $a$  to 0 and this results in a minimization function of,

$$d_{i,j} = \frac{\Delta_{ij}^2}{R^2} \quad (2.14)$$

which makes it independent of particle momentum and sensitive to PU and UE. Due to the fact that the Cambridge/Aachen algorithm is only dependent on the particle coordinate it is most useful in studying jet structure.

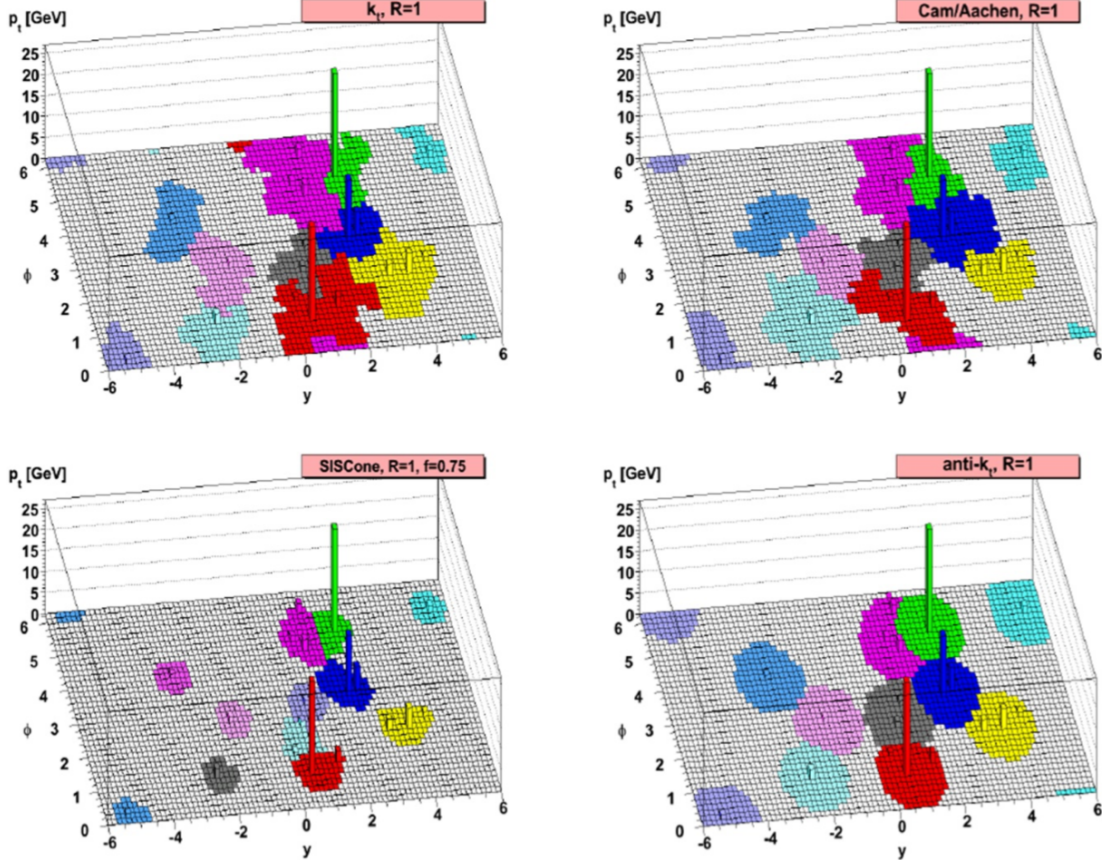


**Figure 2.10:** Lego plot of all four jet finders used on a single event with  $R = 1$  jet radius[21].

Figure 2.10 shows the jets found in a single event using all four jet finding algorithms. It should be noted that the Cambridge/Aachen and  $k_T$  algorithms have highly irregular and large shapes, making them both susceptible to the presence of a UE, while SIScone finds an additional jet due to splitting. The Anti- $k_T$  algorithm finds circular jets which demonstrates its robustness to hard radiation.

Once a stable jet is found, a recombination scheme is deployed in order to garner the jet kinematics. By adding the 4-vector,  $\mathbf{p}^\mu = (\mathbf{E}, \mathbf{p}_x, \mathbf{p}_y, \mathbf{p}_Z)$ , for all of the associated particles

composing a jet, we may obtain the jet momentum, energy, coordinates, etc<sup>3</sup>. In a particle collider with the tracks from a tracking detector measuring particle momentum and the towers of a calorimeter measuring particle energy we obtain the following relationships

$$p_T^{jet} = \sum_{particles} p_T = \sum_{tracks} p_T \quad (2.15)$$

$$E^{jet} = \sum_{particles} E = \sum_{towers} E \quad (2.16)$$

$$\eta^{jet} = \frac{1}{2} \ln \left( \frac{|\mathbf{p}^{jet}| + p_L^{jet}}{|\mathbf{p}^{jet}| - p_L^{jet}} \right) \quad (2.17)$$

$$\tan \phi^{jet} = \frac{p_y^{jet}}{p_x^{jet}} \quad (2.18)$$

where  $p_L$  refers to the longitudinal momentum which is the momentum component parallel to the beam axis. This method of adding the 4-vector of the particles composing the jet together in order to gain the jet kinematics is known as the E-scheme[24].

### 2.3.3 FastJet

FastJet[24] is a C++ software package that performs jet finding. Due to the computational efficiency, ease of use, and straight forward implementation, FastJet is the de-facto preferred jet finder used by theoreticians and all current high energy experiments. It implements the four previously discussed jet finders along with both the E-scheme and a boost invariant  $p_T$  scheme (BIpt-scheme) for recombination. The BIpt-scheme obtains the jet momentum and energy in the same manner as the E-scheme but uses a weighted average to find the jet coordinates,

$$\eta^{jet} = \sum_{particle} \frac{p_T^{particle}}{P_T^{jet}} \eta^{particle} \quad (2.19)$$

---

<sup>3</sup>For a review of relativistic kinematic see Appendix ...

$$\phi^{jet} = \sum_{particle} \frac{p_T^{particle}}{P_T^{jet}} \phi^{particle} \quad (2.20)$$

In addition to basic jet measurements, FastJet contains a number of advance features, which allows it to be used to study jet area, jet substructure, and jet background subtraction[25].

## 2.4 Monte-Carlo Generators

Monte-Carlos (MC) allow for the simulation of high energy events on a statistical basis. Particle level generators use different phenomenological models of the factorization theorem in order to simulate the energy, momentum, particle species, multiplicity, and direction of travel expected in a high energy collision. In order to validate an analysis the particle level simulations are further propagated through a detector level simulation of an experiment, such as Geant3[26], in order to negate detector effects on the output observables from the MC simulation. In this section only the particle level simulations used in the thesis are discussed.

### 2.4.1 PYTHIA

PYTHIA[27], is a C++ Monte Carlo software tool-kit used to model proton-proton collisions. The package uses pre-defined parton distribution functions as input afterwards it simulates the partonic showers and radiation due to a hard scattering by generating the LO scattering matrix elements. Hadronization is performed in PYTHIA using the Lund String Model. After which relative branching ratios are used to statistically throw the decay modes of the hadrons until they are stabilized.

PYTHIA underestimates jet production due to the limitations of using LO calculations. Therefore, it uses an arbitrary value (K-factor) to make NLO corrections to the LO cross section. The K-factor is defined as,

$$K = \frac{\sigma_{NLO}}{\sigma_{LO}}. \quad (2.21)$$

NLO corrections to the cross-section will not match experimental results, PYTHIA implements additional phenomenological adjustments used to better match data. PYTHIA encompass these corrections into sets known as ‘tunes’, with PYTHIA 6.4 Perugia-2010 tune being used for this analysis[28].

### 2.4.2 PHOJET

PHOJET is a FORTRAN 77 Monte Carlo simulator used to model proton-proton collisions. It is an alternative to PYTHIA and is better at modeling soft physics processes present in high energy collisions. PHOJET implements the Dual Parton model[29][30] and multiple parton interactions[31] to model soft physics. Hard interactions are implemented in PHOJET using LO scattering elements and it uses PYTHIA for the fragmentation and hadronization phase. Due to its ability to model soft physics, PHOJET is better at comparing to minimum bias<sup>4</sup> data and understanding jet results in a low kinematic range. PHOJET also acts as a benchmark in understanding any bias due to using other MC generators, such as PYTHIA. PHOJET v1.2 is used in this thesis.

## 2.5 The Quark-Gluon Plasma

At the temperatures and pressures typical to the Universe today nuclear matter is confined to a colorless hadronic gas. However, it was theorized that at extreme temperatures, such as those experienced in the early Universe, partons would have undergone a phase transition where by they were no longer bound to a color neutral state. This state of matter would have been analogous to a conventional plasma where by the electrons are no longer bound to a nucleus, thus the state was dubbed the Quark-Gluon Plasma (QGP). The nuclear phase diagram is shown in Figure 2.11 as a function of temperature and the net baryon density. Normal nuclear matter is confined to the bottom left while increasing temperatures and/or densities correspond to the QGP. Modern particle colliders , such as RHIC and the LHC, are able to obtain the densities and temperatures necessary to create a QGP and are likewise shown in the figure. The reason for particle colliders being located at low baryon density

---

<sup>4</sup>Events with a low total transverse momentum and high cross section

is due to the fact that at high  $Q^2$  energies more quark antiquark pairs are produced. This dilutes the total baryon density in the initial system and is more akin to what the early Universe was like.

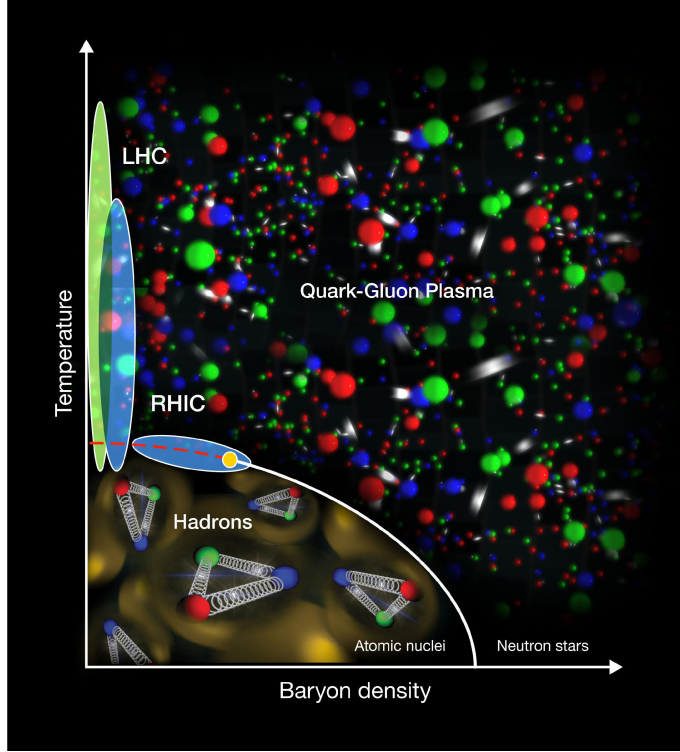


**Figure 2.11:** The QCD phase diagram[32].

### 2.5.1 Nuclear Collisions

By colliding heavy nuclei together in high energy collisions it is possible to obtain the energy densities and temperatures associated with the QGP state. The first signatures for the QGP were measured via a  $J/\psi$  suppression at the Super Proton Synchrotron located at CERN in 2000[33]. In 2005, the four experiments on the RHIC collider: BRAHMS[34], PHENIX[35], PHOBOS[36], and STAR[37], co-announced the observation of a new state of matter consistent with the hot and dense QGP. Surprisingly, the results from RHIC pointed at the QGP behaving more like a perfect fluid over a plasma-like state[38]. The QGP offers a rich and dynamic environment to test QCD predictions under some of the most extreme circumstances. Figure 2.12 shows the difference between a proton-proton collision

and a heavy-ion collision. The heavy-ion collision mirrors the processes in a proton-proton collision (left) described in depth in Section 2.2.1. After the initial hard scattering the phase transition to a QGP occurs. The QGP undergoes a hydrodynamical evolution and expansion until it cools to a colorless hadronic gas. After the phase transition occurs unstable hadrons will decay until they are stable at which point the final state particle composition is set and the chemical freeze out occurs. The hadron gas expands and cools until all soft interactions cease, this is the kinetic freeze out, after which the final momentum spectra is set.

### 2.5.2 Jets as a Probe of the QGP

Jets are an excellent probe of the thermodynamic properties of the QGP. This is due to them being produced in the earliest stages, before the formation of the QGP, and surviving the full evolution of a heavy-ion collision. As a jet propagates through the QGP it will lose energy to the medium through a combination of gluon radiation to the colored medium and inelastic scatterings. These energy loss mechanisms are dependent on the distance a parton travels through the QGP and on the species of the parton.

Figure 2.13 shows two back-to-back partons undergoing a hard scattering. Both will fragment into jets, but the first parton with transverse energy,  $E_{T1}$ , will be subjected to much less energy loss over the second parton due to the first parton only traveling through the outer edge of the QGP. The species dependent parton energy loss arises from kinematic constraints to gluon emission from the heaviest of quarks. This radiation is suppressed at angles smaller than the ratio of the quark mass to its energy and has been dubbed the *Dead-Cone Effect*. Tagging the flavor dependence of jets, either via measuring electrons from semi-leptonic decays or reconstructing the secondary vertex of heavy flavor mesons, has recently shown that energy loss via the Dead-Cone effect is strongly suppressed with jets containing a charm quark[40].

One way of quantifying the energy loss in a heavy-ion collision is via measurements of the nuclear modification factor,  $R_{AA}$ ,

$$R_{AA} = \frac{1}{N_{binary}} \frac{d^2 N_{AA}/dp_T d\eta}{d^2 N_{pp}/dp_T d\eta} \quad (2.22)$$

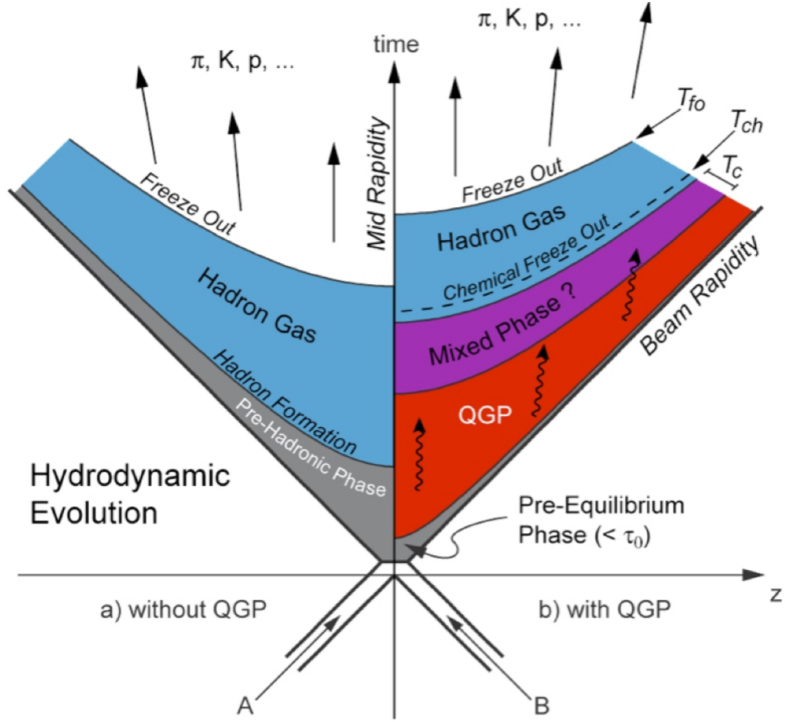


**Figure 2.12:** Comparison between a proton-proton collision with no medium and a heavy ion collision with a colored medium stage[39].

where  $N_{binary}$  is the number of binary collisions and is estimated using a Glauber model[41] of a nucleus while  $d^2N_{AA}/dp_T d\eta$  and  $d^2N_{pp}/dp_T d\eta$  are the spectra measured in nucleus-nucleus and proton-proton collision respectively.  $R_{AA}$  may be thought of as asking the question: Does a heavy-ion collision scale as a superposition of  $N_{binary}$  proton-proton collisions? If a heavy-ion collision simply looks like some  $N_{binary}$  factor of

Figure 2.13 shows the nuclear modification factor with  $R = 0.4$  jets in the ATLAS experiment at 5.02 TeV[42]. The different colored bands in the figure are broken into centrality<sup>5</sup>

---

<sup>5</sup>The purple 10 - 20% band denotes the most central events (i.e. the two colliding nuclei have a low impact parameter and collide nearly head-on), while the 70 - 80% red band denotes the least central events (i.e. the two colliding nuclei have a high impact parameter and barely graze one another). An in depth discussion of centrality may be found here[43].

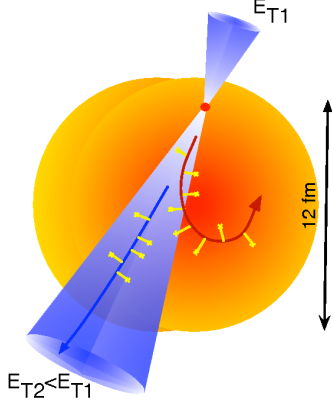


**Figure 2.13:** Jet energy loss in a QCD medium[32].

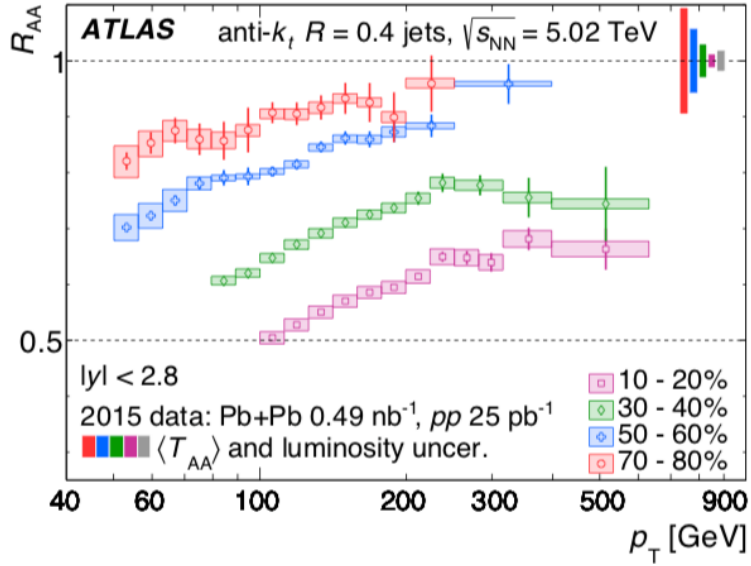


**Figure 2.14:** Jet  $R_{AA}$  at 5.02 TeV with the ATLAS experiment[42].

## 2.6 QGP in Proton-Proton Collisions?

As previously stated a QGP is believed to be absent in proton-proton collisions, thus any signature of a QGP should likewise be absent. However, one way of quantifying the presence of the QGP is via the Bjorken energy density.

$$\varepsilon = \frac{1}{\tau A} \frac{dE_T}{d\eta} \quad (2.23)$$

where  $A$  is the transverse area of the nuclei,  $\tau$  is the proper time, and  $dE_T/d\eta$  is the transverse energy per unit pseudorapidity. It can be shown that the 150 MeV critical temperature need

for the phase transition to the QGP corresponds to 1 - 3 GeV/ $fm^3$  energy density. The quantity  $dE_T/d\eta$  can be related to the mean transverse momentum  $\langle p_T \rangle$  and particle multiplicity<sup>6</sup> per unity pseudorapidity as:

$$\frac{dE_t}{d\eta} \approx \langle p_T \rangle \frac{dN}{d\eta} \quad (2.24)$$

where  $\langle p_T \rangle$  is the mean transverse momentum and  $dN/d\eta$  is the particle multiplicity per unit pseudorapidity. This suggests that in very high multiplicity proton-proton events signatures of the QGP may be present. Although suppression has never been observed in high multiplicity proton-proton collisions physicists have recently measured collective flow in such systems[44]. CMS presented collective flow results in proton-proton collisions at 13 TeV using soft-particles,  $p_T \leq 2$  GeV/ $c$ , consistent with hydrodynamical predictions[45]. These results have opened new debates and questions into the very nature of the QGP and whether jets can be used to enlighten our understanding in such systems will make up a very active and interesting segment of high energy physics research in the coming years.

---

<sup>6</sup>Multiplicity is defined as the number of particles per event

# Chapter 3

## The LHC and ALICE

### 3.1 Overview of the LHC

The Large Hadron Collider (LHC)[? ] is a circular particle accelerator located on the Franco-Swiss border near the city of Geneva. It is operated by the European Organization for Nuclear Research (CERN) and has carried out proton-proton (pp), lead-proton (pPb), and lead-lead (PbPb) collisions at center of mass energies of 0.9-14 TeV, 5.0 TeV, and 2.76-5.5 TeV, respectively. The LHC is approximately 17 miles in circumference and located 200 meters underground. It is located inside the old accelerator tunnel used by the Large Electron-Positron[? ] collider of the 1980's. There are over 8000 physicists and engineers making up the four main experiments at the LHC: ATLAS[? ], CMS[? ], LHCb[? ], and ALICE[? ]. Numerous physics results have been published, with the most famous being the discovery of the Higgs boson in 2012[? ][? ].

Figure 3.1 shows a schematic of the LHC along with the pre-accelerators that help to accelerate protons and ions to their final energies before a collision at one of the four experimental interaction points(IP). Protons are injected into the LHC together in groups called ‘bunches’. Every bunch is comprised of about 120 billion protons with about 50 nanoseconds between the arrival of the next bunch. The bunch scheme during the heavy-ion run is reduced to 200 nanoseconds due to the high multiplicity of the events and additional computational resources needed.

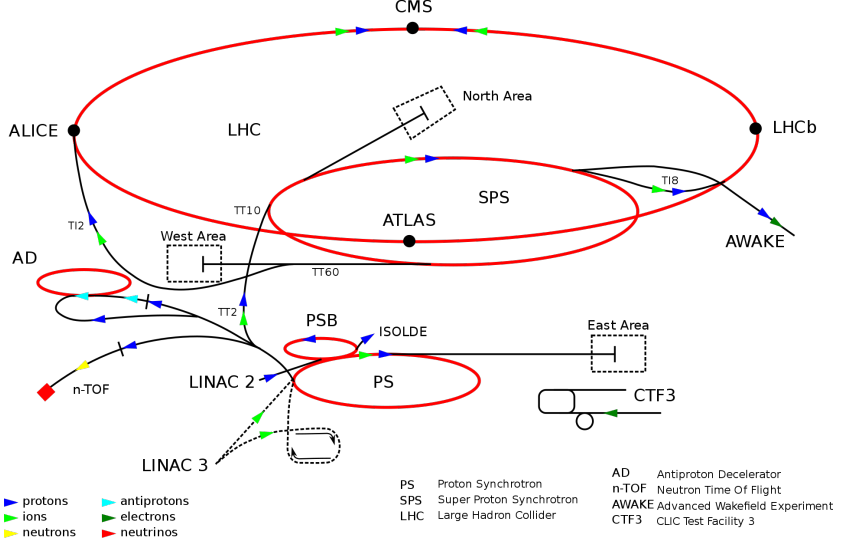


**Figure 3.1:** LHC accelerator complex. The four main experiments are shown in their relative locations[? ].

### 3.1.1 LHC Operations

The LHC first attempted particle collisions in September of 2008. The initial ramping up of the super conducting magnets led to mechanical failure of the helium pipes inside of the LHC beam line. This fault caused the LHC to remain shut down for over a year while the accelerator was repaired and new safety procedures were implemented. The first successful collisions occurred in 2009 with proton collisions at a reduced energy of 0.9 TeV. 2010 marked the beginning of a new era in the high energy frontier with proton collisions at a record setting 7 TeV. The only other major fault that has occurred was in the summer of 2016. A stone marten chewed through a high voltage line in a power transformer on a ground level building at the LHC. The LHC went offline for about a week while repairs occurred and quickly resumed the physics program. Unfortunately, the marten did not survive.

The typical operating year at the LHC allows for any repairs or upgrades on any of the experiments to be performed during the offline period for the first few months. After the offline period the proton physics program begins and lasts until approximately mid-November. The heavy ion program lasts until the first week of December, after which the LHC shuts down for the remainder of the year. From 2014 until early 2015 the LHC was

shutdown for major renovations and upgrades to the accelerator and a number of sub-detectors on each experiment,. This was known as long shutdown 1 (LS1). After 2018, the LHC will go through another shutdown (LS2) during which the accelerator will have a high luminosity (Hi-Lumi) upgrade. This will be discussed in detail along with the upgrades that will be done to ALICE in chapter 4.

### 3.1.2 LHC Accelerator Complex

The LHC accelerator complex is a succession of particle accelerators that increase the energy of particles before they are injected into the next accelerator. Hydrogen atoms are first passed through a high voltage environment that strips any electrons around the nuclei. Once the nuclei are stripped of their electrons they are injected into the linear accelerator(LINAC). The LINAC uses radio frequency cavities to accelerate particles to 50 MeV before they enter the first circular accelerator the Proton Synchrotron(PS). The PS begins to focus the protons into bunches and further accelerates them to 1.4 GeV before the beam enters the Super Proton Synchrotron(SPS). The SPS will further accelerate the particles to 450 GeV. The beam is then injected into the LHC. Once the beams are injected into the LHC they are accelerated to the final collision energy. Afterwards the beams get ‘squeezed’, or tightly focused, with a series of quadrupole magnets. The final step is to ‘adjust’ the two beams to overlap with one another at each experiments IP. Once the adjust phase is completed, collisions will occur at each experiment and data begins to get collected. This entire process from stripping the electrons to having collisions in each IP takes 20 minutes.

In order for the beam parameters to be maintained in the LHC, numerous dipole and quadrupole magnets are deployed to accelerate, focus, and bend the particle beams. The magnets use a superconducting niobium-titanium alloy that are maintained at an operating temperature of 1.9 K using helium-4. Upgrading these magnets is one of the major goals during LS2 as part of the Hi-Lumi upgrade of the LHC[? ].

## 3.2 The ALICE Experiment

A Large Ion Collider Experiment(ALICE) is a general purpose detector that covers a solid angle of  $4\pi$  around the IP. It is 26 m long, 16 m high, 16 m wide, and weighs approximately 10,000 tons[? ]. Like many other large scale detectors ALICE is made up of a number of sub-detectors<sup>1</sup> that perform tracking, particle identification(PID), timing, vertex reconstruction, and calorimetry.

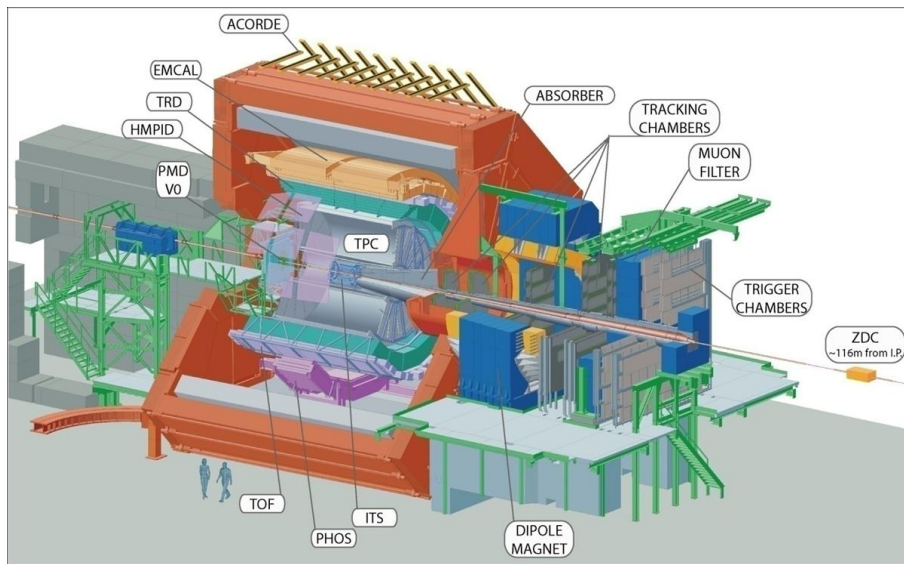


**Figure 3.2:** The ALICE Detector at CERN[? ].

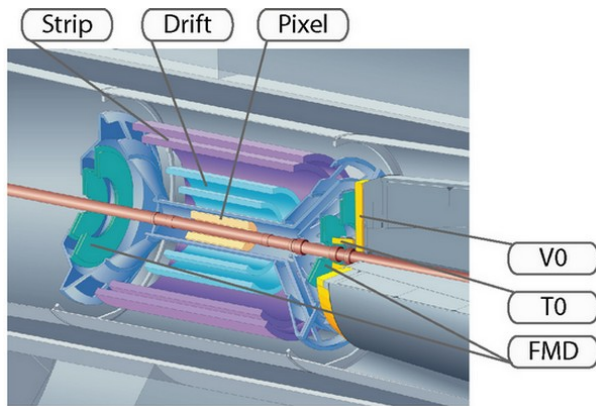


**Figure 3.3:** ALICE tracker, multiplicity, timing, and vertex detectors located near the interaction point[? ].

---

<sup>1</sup>In total ALICE has 18 sub-detectors

Figure 3.2 shows the ALICE detector with human figures to set the scale. Figure 3.3 shows the area closest to the IP with the TZERO, VZERO, Inner Tracking System and Forward Multiplicity Detector; these detectors give basic information on the collision such as vertex location, centrality, timing. Further out from the central region are a number of tracking detectors like the Time Projection Chamber and Time-of-Flight detectors that focus on measuring charged particle momentum and PID. Next are the calorimeters that measure particle and jet energies, such as the Electromagnetic Calorimeter, Photon Spectrometer, and the Dijet Calorimeter. All of these sub-detectors are housed in the L3 magnet seen as the red octagon in Figure 3.2. The L3 magnet provides a uniform magnetic field over the central area of ALICE and is responsible for the high PID performance ALICE has over a wide kinematic region[? ]. At high rapidity, there is a muon tracker and trigger for muon identification. The following sections give a more detailed discussion of the sub-detectors used for this analysis

### 3.2.1 TZERO

The TZERO(T0)[? ] detector is a double layer Cherenkov counter located at 70 cm(T0A) and 370 cm(T0B) from the IP. T0 functions as a trigger and timing detector that determines the precise moment in time at which an event ‘starts’ in the ALICE detector. The timing information from the T0 is fed to other sub-detectors, like the Time-of-Flight and Time Projection Chamber detector, for track reconstruction. The T0 also gives feedback on the target luminosity of the ALICE experiment to the LHC operations center.

### 3.2.2 VZERO

The VZERO(V0)[? ] detector is a double layer scintillator array and similar to the T0 is asymmetrically placed at a distance of 86 cm(V0A) and 329 cm(V0C) away from the primary IP. It provides the ‘minimum bias’(MinBias)<sup>2</sup> trigger information for events and centrality information during the heavy-ion run. Centrality<sup>3</sup> is determined by measuring the

---

<sup>2</sup>A MinBias event is unsurprisingly defined as an event with the least amount of bias possible. Events recorded with a MinBias trigger attempt to not artificially prefer either diffractive or non-diffractive processes over one another[? ].

<sup>3</sup>See Section ??

multiplicity amplitude from the V0 and fitting these results to a Glauber<sup>4</sup> distribution, as seen in Figure 3.4. The V0 is also capable of precision measurements of the target luminosity in the ALICE detector.

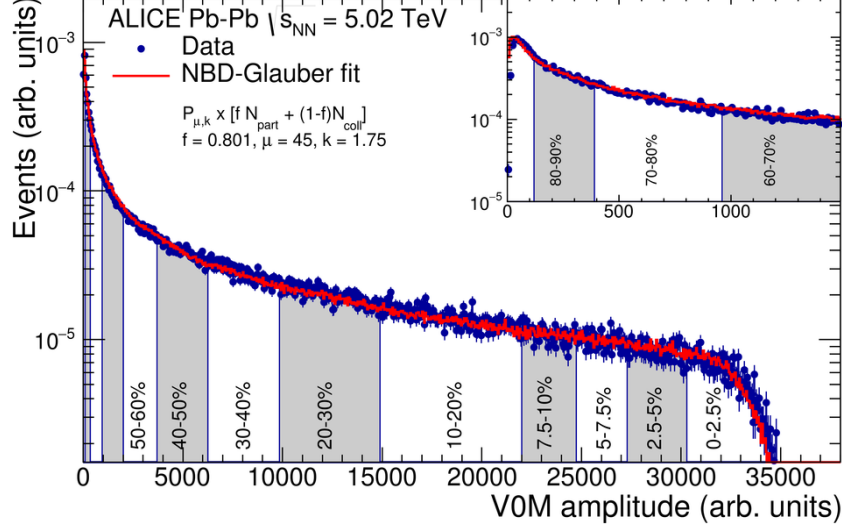


**Figure 3.4:** Multiplicity measured in the V0 detector with Glauber fits corresponding to centrality[? ].

### 3.2.3 Inner Tracking System

The Inner Tracking System(ITS)[?] is six layers of solid state silicon detectors. Closest to the beam line are two layers of Silicon Pixel Detectors. The next two layers are Silicon Drift Detectors and furthest from the beam line are two layers of Silicon Strip Detectors. The main purpose of the ITS is to perform momentum measurements, PID, and vertex reconstruction of charged tracks. PID<sup>5</sup> is performed by measuring the ionization energy,  $\frac{dE}{dx}$ , of charged particles as they traverse the detector[? ]. The ITS has a spatial resolution of  $100 \mu\text{m}$ . This allows for measurements of short lived hadrons by reconstructing secondary vertices, which is the distance of closest approach a track has to the primary vertex.

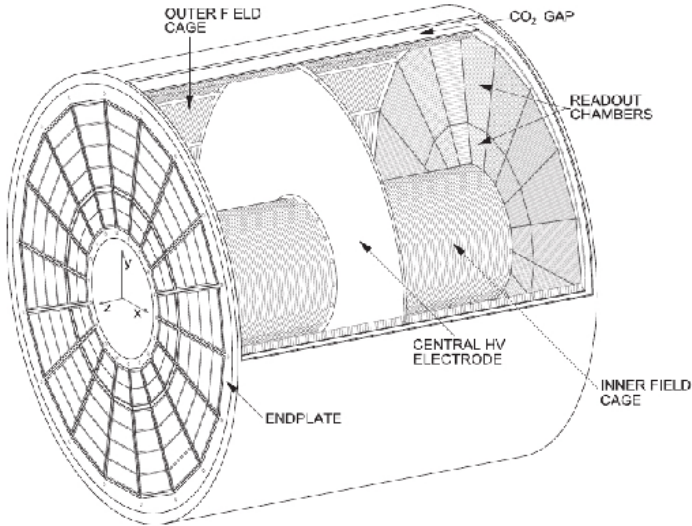


**Figure 3.5:** The ALICE Time Projection Chamber[? ].

### 3.2.4 Time Projection Chamber

The Time Projection Chamber(TPC)[? ] is a gaseous charged particle tracker and the largest of its kind in the world. The TPC has full azimuthal coverage, a pseudorapidity acceptance of  $|\eta| \leq 0.7$ , and a volume of  $93 m^3$ . Figure 3.5 shows a schematic of the TPC. As charged particles traverse the drift volume of the TPC, they ionize the gas inside<sup>6</sup>. A central cathode in the TPC with a voltage of 100 kV induces a uniform electric field of 400 V/m along the beam axis throughout the drift volume. Ionized electrons will drift down to the cylindrical endcaps of the TPC where the read-out chambers(ROC) are located. There are 18 ROCs on each side of the TPC which are further broken into a Inner Read Out Chamber(IROC) and Outer Read Out Chamber(OROC).

#### The TPC readout

The TPC incorporates a Multi-Wire Proportional Chamber(MWPC) design for amplification and copper pads for readout<sup>7</sup>. Ionized electrons created from charged particles take approximately  $100 \mu s$  to move from the drift volume to the readout region. Once these

---

<sup>4</sup>A Glauber model treats the nucleons composing a nucleus as hard shells, more can be found here [? ].

<sup>5</sup>See Appendix ??

<sup>6</sup>The TPC has operated with  $Ne - CO_2$  (90-10) and  $Ar - CO_2$  (90-10) gas mixtures in the past

<sup>7</sup>Their are 72 MWPCs and 500K copper pads in the ALICE TPC

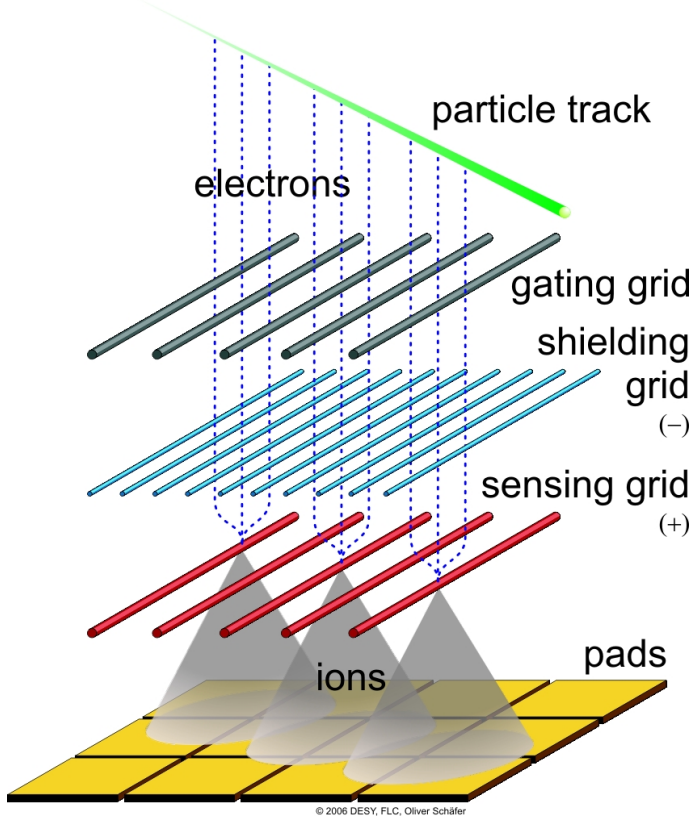


**Figure 3.6:** The TPC readout region[? ].

electrons enter the readout region they will undergo an amplification process with the MWPC, seen as the sensing grid wires in Figure 3.6. This amplification process will turn the few dozen ionization electrons generated from a charged particle into thousands of amplification electrons that are easily sensed by the cooper pads and read from the front-end electronics(FEE). Amplification using MWPCs has the disadvantage of creating thousands of ions known as ‘backflow ions’ that can move back into the drift volume of the TPC. The presence of backflow ions in the drift volume of the TPC will cause distortions in the uniform electric field of the TPC. These distortions are known as ‘space-charge’ distortions and will compromise the physics performance of the TPC. In order to minimize the space-charge distortions the TPC incorporates a gating grid[? ]. Once an event is detected in the readout electronics of the TPC a high voltage is induced on the gating grid. This will capture any backflow ions moving from the amplification region to the drift volume. When engaged the gating grid introduces a dead time as any ionization electrons from new events occurring in ALICE will also get captured. The current configuration of the gating grid is

designed to engage it for 300  $\mu\text{s}$  after an event is first detected. This has been shown to absorb approximately 99% of the backflow ions created while preserving the TPC physics performance. The deadtime due to the gating grid along with the drift time for charged particles in the TPC limits the readout to 3.5 kHz. Upgrading the triggered operation of the current TPC to a continuous readout for the Hi-Lumi upgrade of the LHC will be discussed in detail in Chapter 4.

## TPC Performance

In order to reconstruct the trajectory of a particle, an iterative process known as the Kalman filter approach is deployed. The x-y coordinate which is perpendicular to the beamline are determined via the signal induced on the copper pads. The z component which is parallel to the beamline is reconstructed using the timing information from the T0.

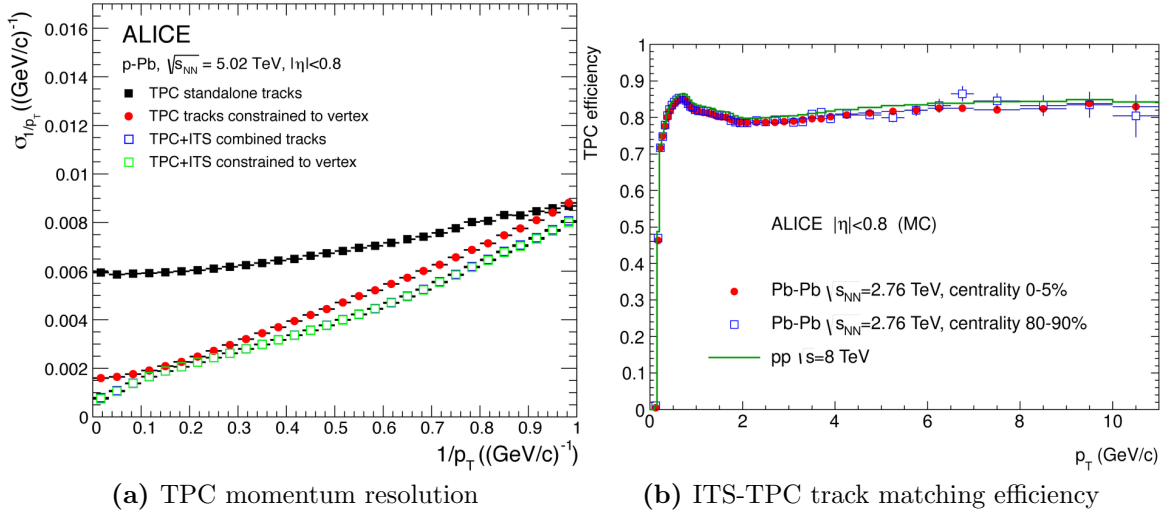


**Figure 3.7:** TPC momentum and tracking resolution[? ].

The TPC has excellent momentum resolution between 150 MeV/ $c$  to 100 GeV/ $c$ [? ]. Figure 3.7a shows the inverse momentum resolution as being below 10% in black. The momentum resolution was further improved to almost 5% over the full kinematic range by matching TPC tracks to ITS tracks and constraining those tracks to originate from the primary vertex region, red and green respectively. The matching efficiency between ITS tracks to TPC tracks is stable at about 80%, Figure 3.7b.

### 3.2.5 Electromagnetic Calorimeter

The Electromagnetic Calorimeter(EMCal)[?] is a lead based sampling calorimeter located at a radius of 4.5 meters from the beam pipe. It covers a pseudorapidity of  $|\eta| \leq 0.7$  and has azimuthal coverage of  $\Delta\phi = 107$  deg.

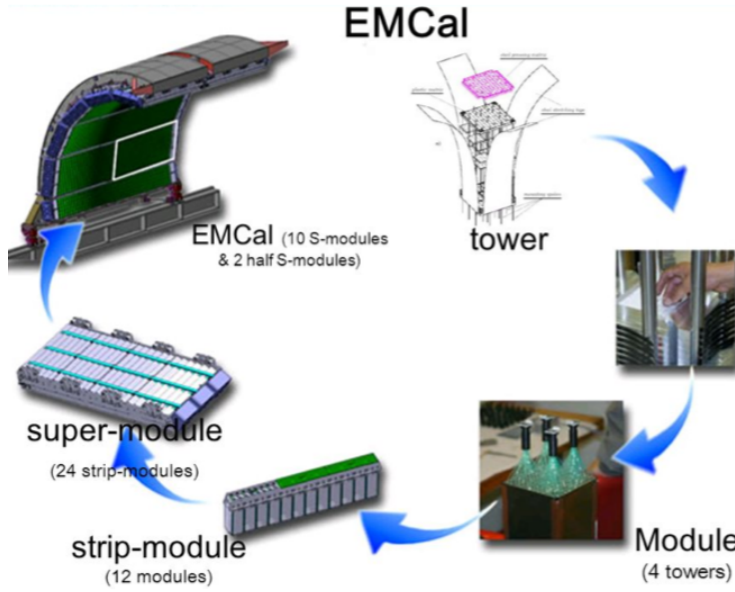


**Figure 3.8:** ALICE EMCal along with super modules, tower strips, and towers[? ].

Figure 3.8 shows the layout of the EMCal. The smallest element of the EMCal is the ‘tower’<sup>8</sup>. The tower serves as the readout and is made up of several layers of alternating scintillator and Pb-absorber. Particles that interact via the electromagnetic force initiate a shower in the absorber material in the tower. This electromagnetic shower induces light in the scintillator to accumulate in the avalanche photodiodes(APD) in proportion to the particle’s energy. A ‘module’ is an array of four towers that share readout electronics. Twelve modules will be placed in a single strip that provides support to the structure. The largest component of the EMCal is the super-module, consisting of 1,100 towers, which serves as the mounting structure to the ALICE detector. In 2015 Dijet Calorimeter(DCAL) was installed in the ALICE detector to perform back-to-back jet measurements.

---

<sup>8</sup>There are 12K towers in the EMCal

## EMCal Performance

As particles enter the EMCal they initiate an electromagnetic shower. The shower of electromagnetic particles spans several neighboring towers, these towers are grouped together into ‘clusters’ and the Analog-To-Digital Conversion(ADC) signal from the clusters corresponds to the energy deposited by the particle. The EMCal was designed so that photons and electrons will fully shower inside of the tower region and thus fully deposit their energy. Hadrons on the other hand will punch through the EMCal and only deposit a small fraction of their energy. PID can be performed using the EMCal via track-cluster matching from the TPC. TPC tracks are geometrically matched to the centroid of a cluster and if no track is matched the cluster originated from a photon. If a track is matched, then the ratio of E/P, the energy of a matched cluster to the momentum of a TPC track, can be used to separate electrons from hadrons.

The energy resolution of the EMCal follows the form seen in equation 3.1

$$\frac{\sigma}{E} = \sqrt{A^2 + \frac{B^2}{E} + \frac{C^2}{E^2}} \quad (3.1)$$

where E is the cluster energy, A characterizes stochastic fluctuations such as photon collection efficiency, B is a function of the systematic effects such as detector non-uniformity, and C is a function of the noise in the Front-end electronics.

As seen in figure 3.1 excellent agreement exists between the measured performance of the EMCal compared to simulations in a kinematic range between  $10\text{GeV} - 100\text{GeV}$ . The stochastic term, A, is the largest source of uncertainty in the energy resolution due to the EMCal being a sampling calorimeter. Unlike the TPC the resolution improves at high- $p_t$  making the EMCal ideal for measuring high energy particles and jets

## EMCal Trigger

Due to the high luminosity in the LHC only a small fraction of events may be recorded to disk for later analysis. ALICE employs a variety of triggers to record events that have the highest value for performing quality physics analysis. The EMCal can trigger on events in order to increase the effective sample size for high- $p_T$  jets, photons, and electrons. The two

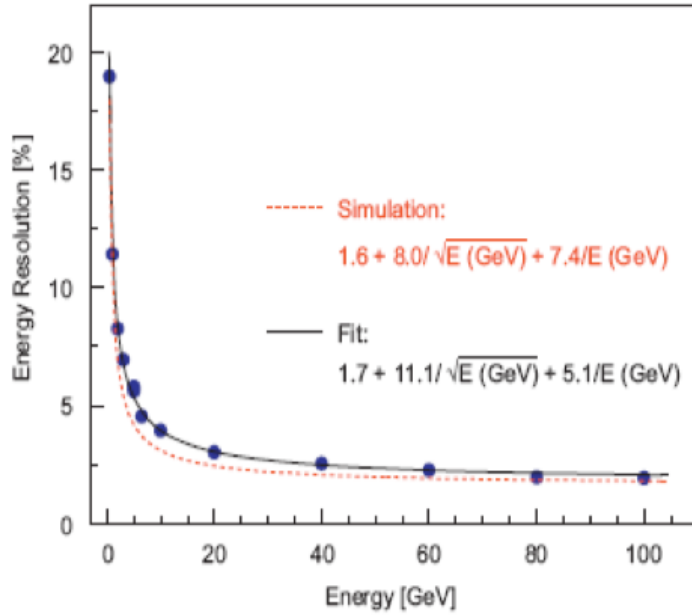


**Figure 3.9:** Energy resolution in the EMCal measured in a 2007 test beam at CERN(blue) compared to GEANT3 simulations of the EMCal(orange), fits for the parameters A, B, and C are also shown[? ].

main triggers[? ][? ] for the EMCal are a jet trigger and a gamma trigger. The gamma trigger is comprised of a 4x4 patch of EMCal towers, while the jet trigger is a 16x16 patch of towers. Once the gamma trigger has surpassed a minimum energy threshold of 5 GeV[?] the event is tagged as a gamma event and the patch location is recorded.

EMCal jet triggered events have an energy threshold of 20 GeV and are similarly tagged and recorded. Figure 3.10 shows the spectra from clusters measured in the EMCal using MinBias data in black and the gamma trigger from the EMCal set to two thresholds, 5 GeV and 7 GeV. Recording the events that satisfy the EMCal triggers introduces a bias towards high- $p_T$  processes, however by using events that had an EMCal trigger we can extend the kinematic range of an inclusive jet measurement as seen in Figure 3.10. In order to account for this bias it is necessary to calculate a trigger efficiency by comparing spectra from inclusive jets recorded using the MinBias trigger to the spectra generated from the EMCal triggers. The calculation of the trigger efficiency will be discussed in depth in section ??

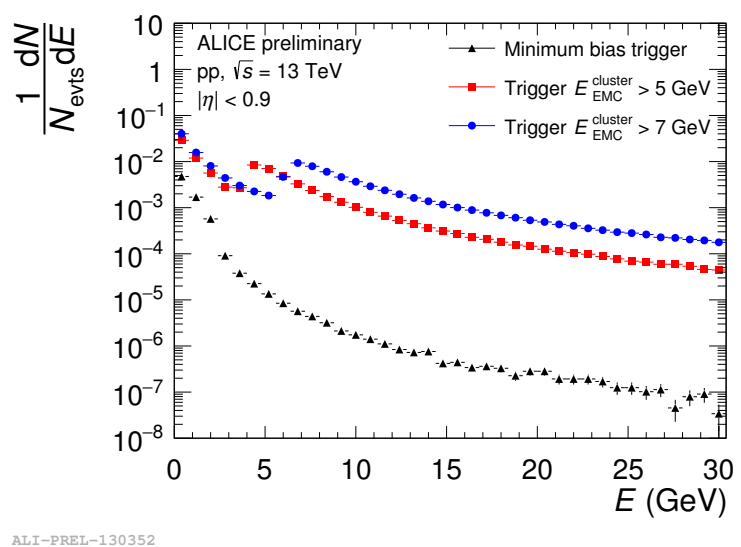


**Figure 3.10:** Cluster Spectra from the ALICE EMCal. MinBias is shown in black while the red and blue points show the spectra using the gamma trigger at two energy thresholds[? ].

# Chapter 4

## The ALICE TPC Upgrade

From 2014 until 2018, I worked on the upgrade of the TPC to a continuous readout. This includes working on a test beam in 2014 for a prototype Read-Out Chamber (ROCs) using Micropattern Gaseous Detectors (MPGD) over the current Multi-Wire Proportional Chamber (MWPC) design. Once a final design for the new ROCs was chosen the production of the new Inner Read-Out Chambers (IROCs) using a stack of four Gaseous Electron Multiplier (GEM) foils took place at the University of Tennessee. During this period I assembled 49 new IROCs. In 2018, I traveled to Yale University and CERN to help with quality assurance of the IROCs built at Tennessee.

### 4.0.1 Physics Motivation

After the 2018 heavy-ion run ends, the LHC will begin the second long shutdown (LS2) and upgrade to the High Luminosity LHC (Hi-Lumi LHC)[? ] which was briefly mentioned in section 3.1. The goal of the LHC upgrade is to move into an era of high precision measurements of rare QCD processes and increase the production of soft probes. Once the upgrade is complete the expected event rate in ALICE will be 50 kHz in MinBias PbPb collisions. This will lead to a factor of x100 increase in MinBias data and a factor of x10 increase in high- $p_T$  triggered data recorded by ALICE.

The ALICE experiment has focused on probing the thermodynamic properties of the QGP in the past. The increase in event rate expected from the Hi-Lumi LHC would open new ways to probe the QGP including[? ]:

- Increasing the production of jets and allowing separation of jet measurements based on the flavor of the initial parton.
- Studying the production mechanisms of light-nuclei, antihyper-nuclei, and other exotic hadrons.
- Probing the initial state temperature and equation of state of the QGP by measuring low-mass dileptons that originate from the earliest stages of a heavy-ion collision.
- Increase the yields of heavy-flavor mesons reconstructed via the secondary-vertices.

In order to do this ALICE will implement a number of upgrades [? ] during the shutdown that include:

- Replacing the V0 and T0 detectors with a combined detector, called the Forward Interaction Trigger (FIT)[? ].
- Improving the ITS and Muon Tracker spatial resolution by using Monolithic Active Pixel Sensors (MAPS)[? ][? ].
- Removing the 400 nanosecond dead time associated with the TPC and upgrade the FEE cards to handle the increase in data bandwidth[? ].
- New Online/Offline ( $O^2$ ) data processing architecture[? ].

Leptons weakly couple to the QGP[? ] and by studying these the initial states in heavy ion collisions may be probed[? ]. Figure 4.1 shows a simulation of the mass spectra for dileptons between  $0 \text{ GeV}/c - 1 \text{ GeV}/c$  using the current ALICE central detectors with tight kinematic cuts (left). The yields that are quantifiable do not allow for the separation of leptons originating from the QGP from those originating from background sources. After the increase in event rate and the upgraded ITS with improved tracking capabilities, measuring

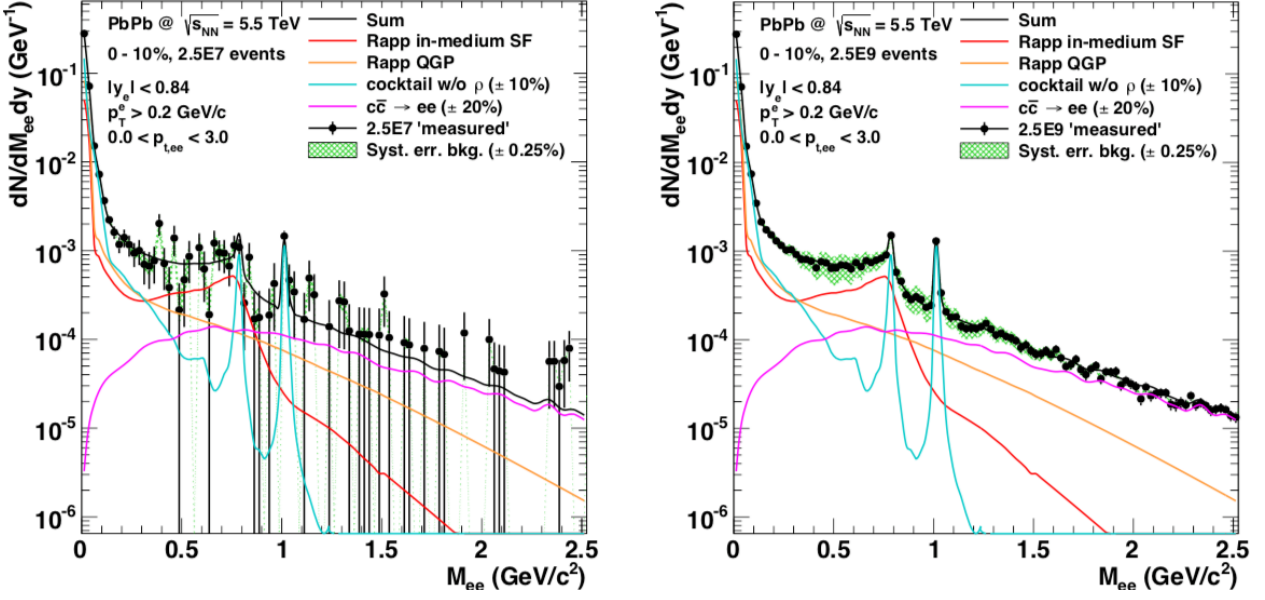


**Figure 4.1:** Simulation of the invariant mass spectra for dileptons in a typical heavy-ion run with current ALICE performance (left) and after upgrade of ALICE for Run-3 (right) in PbPb at  $\sqrt{s_{NN}} = 5.5$  TeV. The dilepton yields originating from the QGP are shown (red and orange), along with background contributions from light-hadrons (blue), and charm (magenta)[? ].

the low-mass dileptons that interacted with the QGP will be possible as shown on the right of Figure 4.1.

The TPC used in the ALICE experiment along with the readout was discussed in section 3.2.4. The ALICE collaboration first proposed an upgrade of the TPC in 2012 with a Letter of Intent (LoI)[? ]. A Technical Design Report(TDR)[? ] was published in 2013 with an initial design overview. An addendum to the TDR[? ] was published in 2015 after the performance of prototype ROCs was measured on a test beam at CERN in 2014. The overall goals of the TPC upgrade are to continuously readout events in the high luminosity environment expected after LS2, to minimize the accumulation of space-charge distortions in the drift field, and to maintain the PID and tracking performance of the current TPC.

#### 4.0.2 Gaseous Electron Multiplier Foils

Gaseous Electron Multiplier (GEM) Foils were first proposed by CERN physicist Fabio Sauli in 1997[? ]. GEMs belong to a new form of detector technology known as Micropattern

Gaseous Detectors[? ] that use microelectronic or chemical etching techniques to print a readout structure onto a material surface.

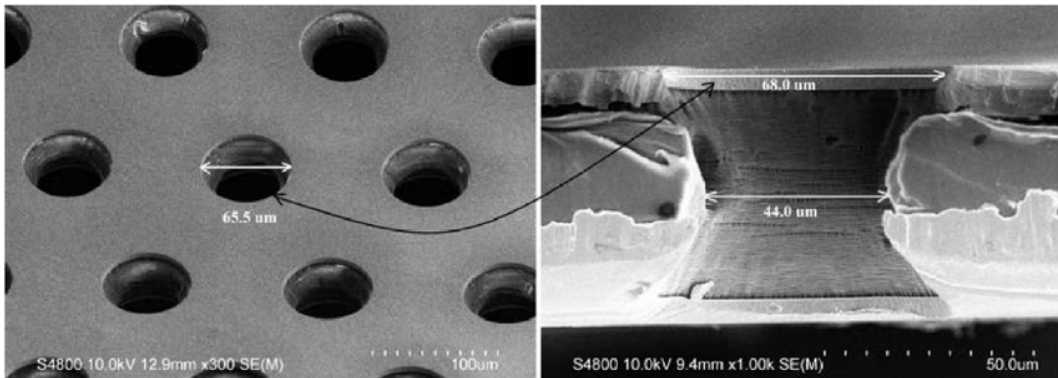


**Figure 4.2:** Scanning electron microscope image of a GEM foil from top (left) and profile (right)[? ].

GEM foils are a Kapton sheet, typically  $50 \mu m$  thick, with a thin copper coat on both sides of the surface. A weak acid and stencil are used to chemically etch holes throughout the foil. Typically, the holes are between  $10 \mu m$  -  $100 \mu m$  in diameter and between  $100 \mu m$  -  $300 \mu m$  in pitch as seen in Figure 4.2. A few hundred volts is applied to each of the copper surfaces of the GEM foil causing a strong electric field to be induced in the GEM holes<sup>1</sup>.

When a ionization electron from a charged track enters a GEM hole it will cause an avalanche of electrons and ions to be produced, amplifying the signal, to MWPCs. Due to the high voltage and strong electric fields around the GEM foil, any back flow ions created from the avalanche will get absorbed by the copper surfaces on the GEM foil, as seen in Figure 4.3.

The configuration of the pitch and size holes on a GEM foil is directly correlated to the amplification properties and ability to capture back flow ions. GEMS with larger holes or shorter pitch between the holes will have more amplification but will also be more ineffective at capturing ions. Likewise, GEMs with shorter holes or larger pitch will have better ion capture abilities yet worse amplification properties. By stacking multiple GEMs on top of one another it is possible to maximize the amplification properties and minimize the backflow.

Creating GEMs with a uniform hole distribution and stacking them in a consistent manner in order to minimize the overlap of holes from one layer to another restricted

---

<sup>1</sup>The electric field is on the order of  $10 \text{ kV/cm}$

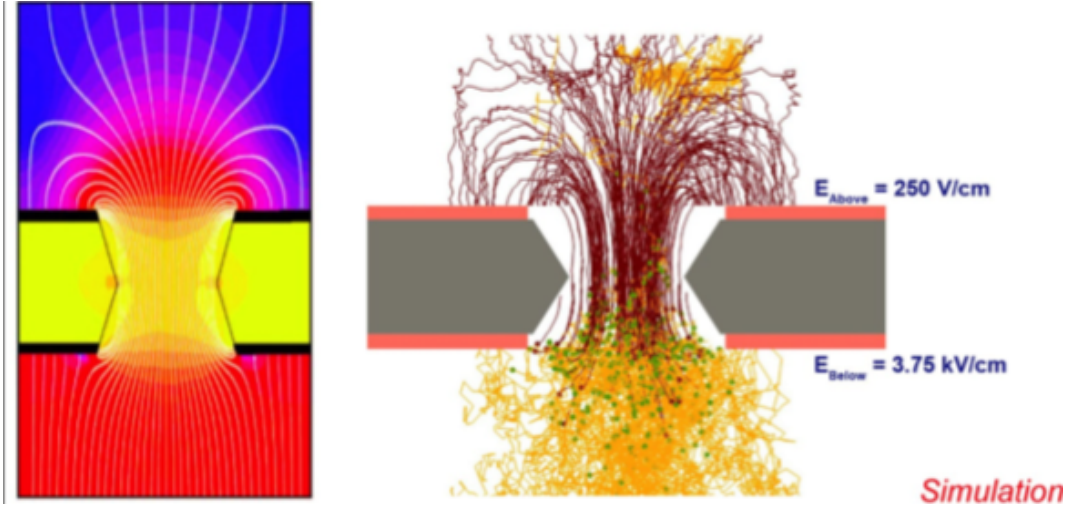


**Figure 4.3:** Profile of GEM with electric-field lines and gradients (left). Simulation of an ionization electron (yellow line) entering a GEM from a drift volume, amplification electrons (green dots, yellow lines) and back flow ions (red lines) are created (right)[? ].

them to small prototypes and impeded their use on large experiments. Around 2010 two methods were developed, the single-mask technique[? ] and the NS2 assembly[? ], which allowed for a systematic way of etching holes and stretching GEMs so they could be properly aligned. These methods allowed for GEMs to become a viable amplification device for large experiments. As of 2018 the TOTEM, COMPASS, ATLAS, and LHCb experiments have all incorporated GEMs in their trackers. Future colliders, such as the Electron-Ion Collider (EIC), plan on using them[? ].

#### 4.0.3 Research and Development

Initially, it was decided that the new ROCs would incorporate a stack of three GEMs with a hole geometry similar to the one incorporated on the LHCb experiments[? ] tracking detector. This was a starting point to bench mark performance for the ALICE TPC upgrade as well as an opportunity to use experts in GEM technology already present at CERN. The first phase of the R&D involved simulating the performance of the LHCb 3-GEM stack in the high event rate environment expected after the Hi-Lumi LHC upgrade using a the software package called Garfield++[? ], which is a GEANT4[? ] add-on package built to simulate MPGDs. It was quickly observed from the simulations that a 3-GEM stack would

be insufficient in maintaining the performance needed for the TPC while minimizing the ion back flow. An additional layer of GEM was added to the 3-GEM stack in simulation and it was observed that this configuration would preserve the TPC performance.

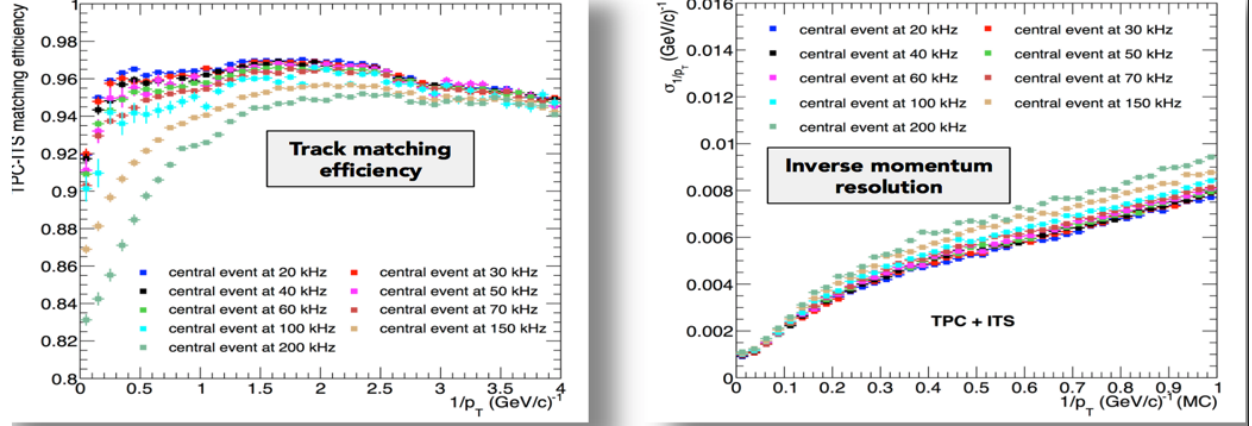


**Figure 4.4:** ITS-TPC matching (*left*) and inverse momentum resolution (*right*) for a 4-GEM stack simulated in Garfield++ [? ].

Figure 4.4 shows simulations of the track matching efficiency from the ITS to the TPC and the inverse momentum resolution for a 4-GEM stack as a function of several collisions. The efficiency and resolution only start to diminish at an event rate above 100 kHz, which is double the expected rate after the LHC upgrade, and are well within the range of the current TPC operating at 3.5 kHz.

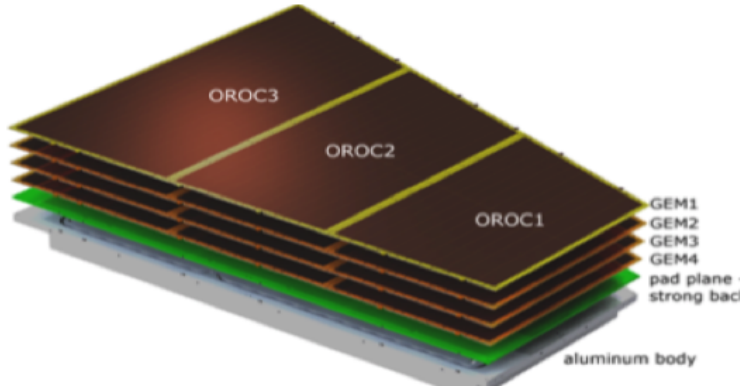


**Figure 4.5:** Final design of the upgraded readout chambers with a stack of 4 GEMS [? ].

The optimal hole configuration was also explored with simulations. Having a first and forth layer with a pitch of 140  $\mu m$  and the second and third layer with a pitch of 280  $\mu m$ , allowed for the the ROCs to maintain minimal ion backflow while amplifying the signal from

tracks. Figure 4.5 shows the design of the ROCs with a 4-GEM stack. The copper pad plane is glued to a reinforced fiberglass sheet, known as the strongback, to add material strength.

## 2014 Test Beam

During the 2014 test beam, I mounted the prototypes on the beam line, recorded data from the test beam, and monitored the performance in real time. To quantify the performances of the prototype, it is useful to define the effective gain ( $G_{eff}$ ) and ionic backflow (IBF%)

$$G_{eff} = \frac{I_{anode}}{e N_{ion} R} \quad (4.1)$$

where  $e$  is the fundamental electric charge of an electron,  $N_{ion}$  is the number of captured ions, and  $R$  is the illumination rate from an active source.

$$IBF\% = \frac{I_{cathode}}{I_{anode}} = \frac{1 + \epsilon}{G_{eff}} \quad (4.2)$$

where  $I_{cathode}/I_{anode}$  is the ratio of the currents measured in the cathode and anode portion of a readout as seen in Figure 3.6. The IBF% can also be defined in terms of the number of backflowing ions ( $\epsilon$ ) created at an effective gain ( $G_{eff}$ ). The effective gain is a measure of the amplification properties and in a gaseous detector is defined as

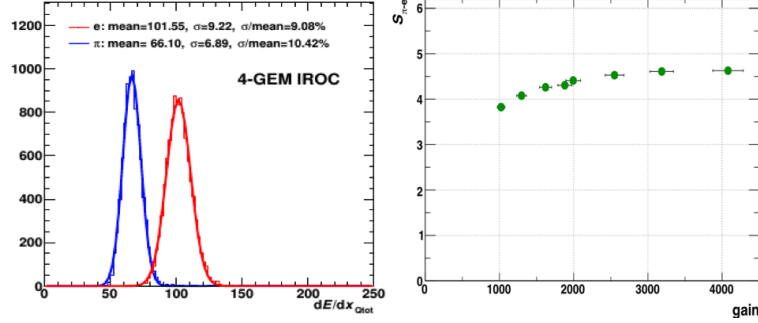
The test involved using the beam from both the SPS and PS<sup>2</sup> at the LHC cast onto an iron target. This iron target created secondary showers and tracks were measured by the prototype for both energy resolution and PID performance. The nominal TPC gas of  $CO_2 - N_2$  (90-10) was used during the test beam.

Figure 4.6 shows the PID performance for separating electron and pion tracks created by the iron target. The separation power between the two Gaussian peaks increases until a gain of 2000 so this was chosen as the target effective gain for the new ROCs.

Figure 4.7 shows the energy resolution of the iron peak as a function of the relative voltages between GEM 2 ( $U_{GEM2}$ ) and the ratio of voltages between GEM 3 ( $U_{GEM3}$ ) and GEM 4 ( $U_{GEM4}$ ). This shows that the IBF% remains below 1% at a energy resolution of approximately 10% which is consistent with the current TPC performance. The voltages

---

<sup>2</sup>See Section 3.1.2.



**Figure 4.6:**  $dE/dx$  resolution of the 4-GEM IROC prototype (*left*) and the separation power between electrons and pions as a function of gain (*right*)[? ].

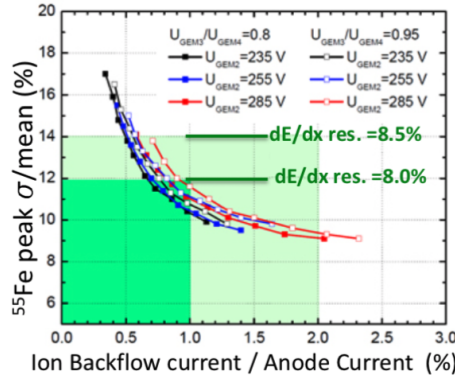


**Figure 4.7:** Energy resolution of the iron peak as measured from the prototype IROC with varying GEM voltages as a function of IBF%[? ].

were chosen such that GEM 1 and GEM2, which are closest to the drift volume, would focus mostly on capturing amplification ions while GEM 3 and GEM 4, which are closest to the copper pad readout, would primarily perform the amplification as shown in Figure 4.8.

#### 4.0.4 Production of the Inner Readout Chambers in the U.S.

Once a final design was settled on from the simulation and prototype R&D, the project entered the production phase. A minimum of 36 new ROCs would need to be built with the 4-GEM stack to replace the old ROCs in the TPC while 4 additional ROCs would be constructed as spares. Due to the size and weight of the ROCs, production of the IROCs would take place in the United States and the OROC production mainly in Germany.

Figure 4.13 shows the production flow for the construction of the 4-GEM ROCs. After GEMs are received from the manufacturer, they go through a number of quality assurance tests

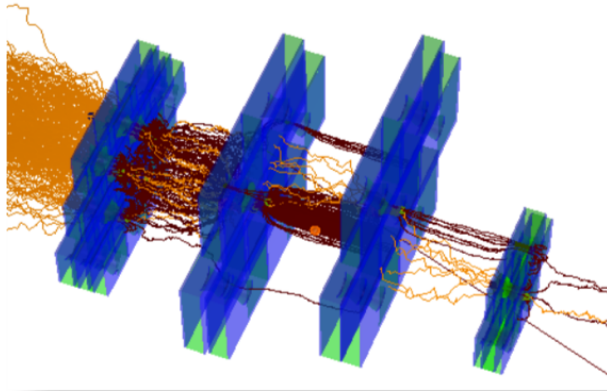


**Figure 4.8:** Simulation of the four GEM (blue) layers after test beam. The configuration is such that the two GEMs closest to the drift volume, right side, absorb the amplification ions created by the two GEMs closest to the readout (right) [? ].

before they are shipped to Wayne State University, where they are stretched and mounted for the IROCs. The aluminum bodies are manufactured at the University of Texas Austin and shipped to Tennessee. At Tennessee we glue the pad plane, aluminum body and strong back together before it is shipped to Yale, where the chambers are fit with the GEMs from Wayne State. The production steps for the OROC mirror those performed by the IROC except that it was performed mainly German institutes.

Figure 4.10 shows the procedure followed at Tennessee in order to build an IROC. Furthest on the left is a picture of a copper pipe glued into the aluminum body. This copper pipe is flushed with a coolant that maintains the temperature of the Front End Electronics (FEE). The next two photos show the pad plane being mounted on a vacuum table while glue is applied to it and the aluminum body. Once all the components are placed glued and mounted on the table the IROC is loaded with lead bricks and allowed to cure for 24 hours. The right most picture shows the final step of the HV feedthroughs mounted and glued for the GEM foils. Before a completed IROC leaves Tennessee we performed a gas tightness test that will be discussed more in the next section. Full production of the IROCs ended in November of 2018 with a total of 47 chambers being built at Tennessee. A surplus of chambers were built with excess materials to provide spares.

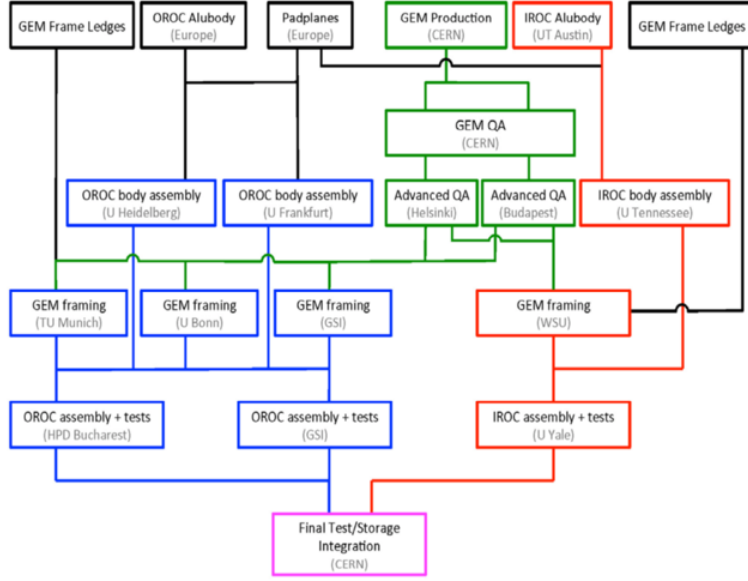


**Figure 4.9:** Production flow of the IROCs (red), OROCs (blue), and GEM foils (green)[? ].



**Figure 4.10:** The author assembling an Inner Readout Chamber at the University of Tennessee.

#### 4.0.5 GEM and Chamber Quality Assurance

A stringent set of quality assurance (QA)[? ][? ] protocols were implemented to monitor any damage sustained during transport and to quickly identify any flaws in the production procedures. The QA can be broken into two major categories: QA performed on the GEM foils as received from the manufacturer and QA performed on complete/semi-complete

chambers as they were going through the different production steps. I will discuss only the QA tasks that I was directly involved with.

## GEM QA

In order to evaluate the performance of a GEM foil, a spark test was performed on every foil. Sparks are caused by the discharge of the foil and may be due to the presence of dust on a foil, imperfections in the hole geometry, or a short between the two copper layers of the GEM. The final design of the GEM foils had each foil segmented into twelve sectors with a  $10 M\Omega$  bias resistor across every segment. Any sparks that occur on the GEM will only discharge a given segment and not the entire foil. Because of the delicate nature of the GEM foil, sparks have the potential to permanently damage a foil or seriously affect the performance of a ROC. Thus GEMs with a high spark rate should be excluded as soon as possible in the production flow.

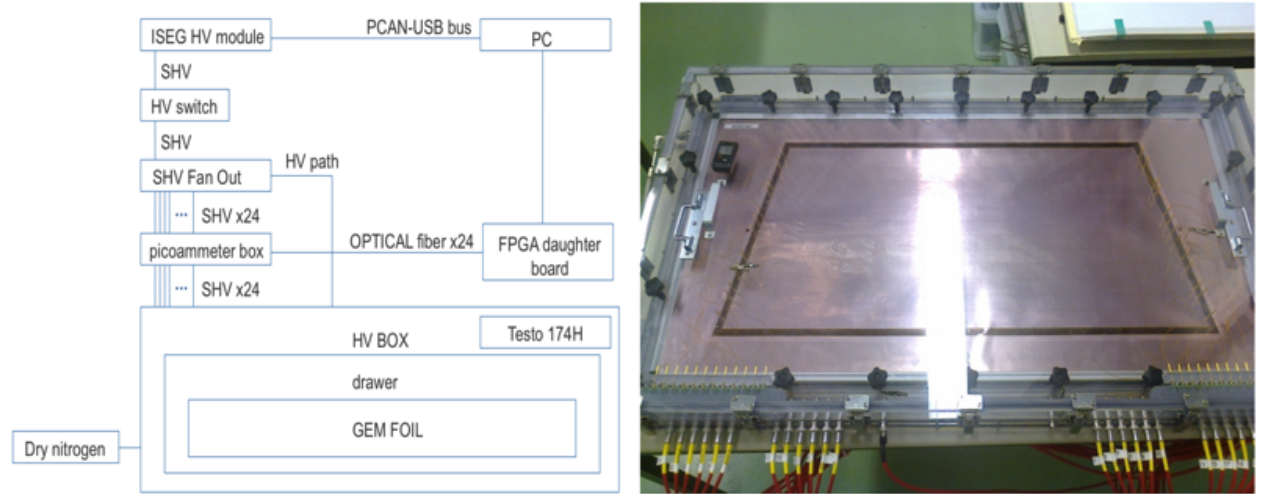


**Figure 4.11:** Schematic for the setup of the GEM foil spark test (*left*)[?] and the GEM mounted in the HV gas box (*right*).

The GEM foil spark test involves mounting each foil in a High Voltage (HV) box, which is flushed with  $N_2$  until it reaches a relative humidity of  $\approx 10\%$ . Once this humidity is reached 500 V is placed across each segment of the GEM and monitored with a LabView interface. A spark is defined as the LabView recording a current above 10 nA across the bias resistor through any GEM segment and read by a multi-channel picoammeter. The criteria for a GEM to fail this QA was to have more than five sparks over a 20 minute recording window.

## Chamber QA

Most of the QA I helped with was on ROC chambers as they went through the production steps. Before completed IROC chambers were sent to Yale, I performed a gas leak test. The leak test consisted of mounting an individual chamber into an aluminum test vessel and flushing the inside of the vessel with  $N_2$  gas. By using a flowmeter to measure the rate that  $N_2$  gas enters the test vessel and an oxygen sensor to measure the amount of oxygen present at the output of the test vessel we can infer the leak rate of each IROC chamber. Figure 4.12 shows a schematic of the setup (left) and what the typical output from the LabView interface (right). By flowing at two different rates and measuring the oxygen content at each rate we could confirm the leak rate.

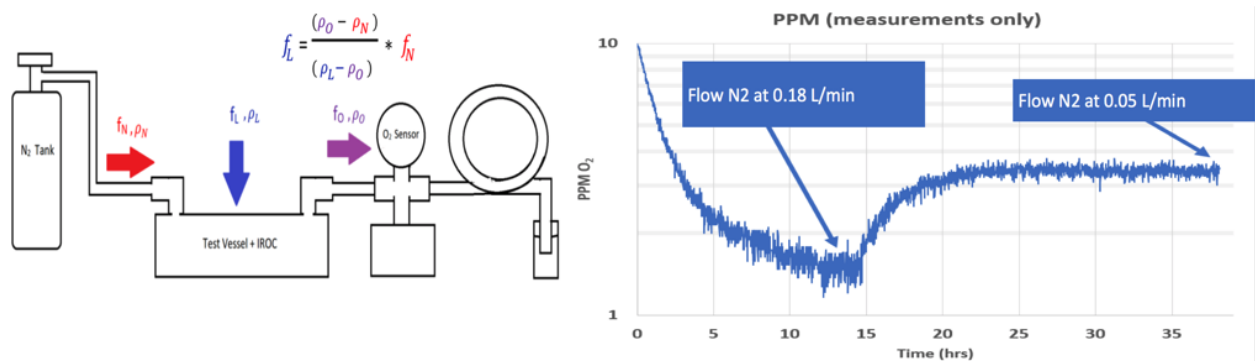


**Figure 4.12:** Schematic of the gas tightness testing setup at the University of Tennessee (*Courtesy of Joseph Rasson*).

The leak rate of a chamber,  $f_L$ , can be quantified as

$$f_L = \left( \frac{\rho_0 - \rho_N}{\rho_L - \rho_0} \right) f_N \quad (4.3)$$

where  $f_N$  is the flow rate of  $N_2$  gas into the test vessel,  $\rho_L$  is the concentration of  $O_2$  in the laboratory,  $\rho_N$  is the  $O_2$  impurity present in the  $N_2$  bottle, and  $\rho_0$  is the  $O_2$  reading from the LabView interface.

A maximum leak rate of 0.25 mL/hour was placed as the rejection criteria for a given chamber. If a chamber had a leak rate above this the  $N_2$  gas could get swapped out with a helium gas tank and we could use a helium sniffer to identify the areas on the IROC

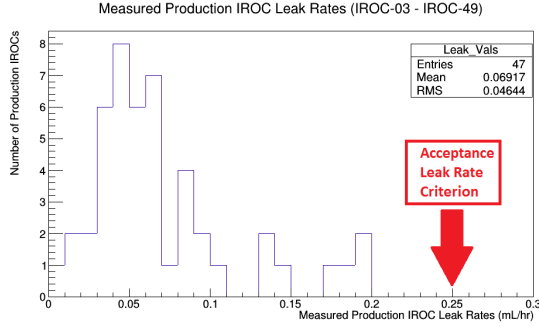


**Figure 4.13:** Leak rate of the 47 chambers built at Tennessee with the maximum failure rate at 0.25 ml/hr shown (*Courtesy of Charles Hughes*).

causing the leak and patch the area with epoxy. Figure 4.13 shows the leak rate for all IROCs produced at Tennessee, due to none of the chambers surpassing the leak threshold the helium sniffer was not used in the production of the IROCs.

Once an IROC chamber was fitted with the 4 GEM foils at Yale and sent to CERN a spark test was performed over the entire chamber. The test involved placing each chamber next to the LHC beam line, flushing with the nominal TPC gas, and placing the nominal voltage across each GEM and monitoring the spark rate once a beam was present in the LHC. Figure 4.14 shows myself installing the completed IROC chambers next to the LHC beam line in front of ALICE and the output from the spark monitor. The voltage across each chamber could be varied in real time in order to minimize sparking while maintaining the IROC performance, thus reducing the rate of degradation on a per chamber basis once installed in the TPC.

#### 4.0.6 Outlook

As of November 2018, the 47 IROCs assembled at Tennessee have been received at CERN. None of the built chambers have surpassed the gas leak test performed at CERN and so far only 4 chambers exhibit sparking rates above the threshold. By May of 2019, the LHC beamline around ALICE will be decommissioned and the TPC will be moved to a surface level clean room for the installation of the chambers. The installation of the new FEE electronics and the ROC chambers should take place throughout the summer of 2019. Afterwards there will be a 10 month commissioning with the TPC, during which the performance of the

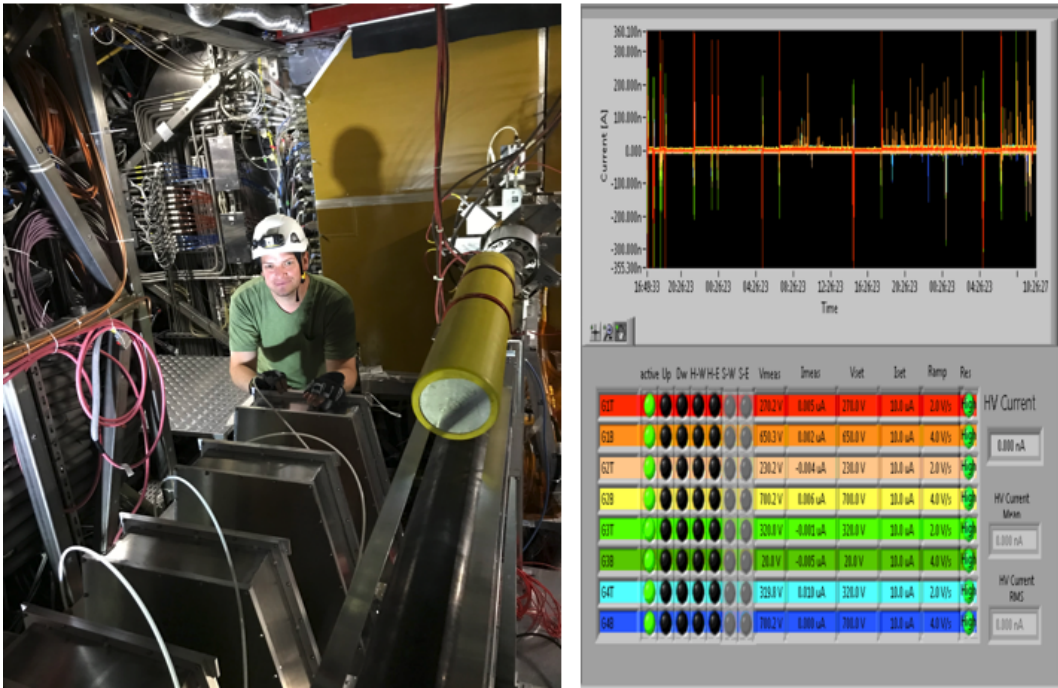


**Figure 4.14:** The author testing spark testing chambers next to the LHC beam line (*left*) and real time output from the spark test during a live beam (*right*).

upgraded TPC will be evaluated with cosmic rays. By the end of 2020, the TPC should be back in the ALICE cavern and the beam line will have been re-installed. The Hi-Lumi run of the LHC is expected to start in March of 2021.

# Chapter 5

## Jet Results and Discussion

Beginning in March of 2012, the LHC began seven months of pp collisions at  $\sqrt{s} = 8$  TeV. The jet cross sections and ratios of the cross sections for jets of different radii offers a unique perspective on the pQCD effects of hadronization at this new energy frontier. Due to the expectation that no QGP is formed in a pp collision these measurements serve as a baseline for separating phenomena associated with the QGP in heavy-ion collisions. In order to measure the jet cross section the following formula is used,

$$\frac{d^2\sigma^{jet}}{d\eta dp_T} = \frac{A_{trigger}}{\epsilon_{trigger}(p_T)} \times C_{MC} \times \frac{1}{A(p_T)} \times \frac{1}{\mathcal{L}_{int}} \times \frac{dN^{jet}}{dp_T d\eta} \quad (5.1)$$

where,

- $A_{trigger}$  is the acceptance for EMCal triggered events and  $\epsilon_{trigger}(p_T)$  is the EMCal trigger efficiency. These factors correct for imperfections in the electronics of the EMCal and the overall factors are equal to one in minimum bias events.
- $C_{MC}$  is a correction factor due to detector effects and it allows for comparisons between the ALICE experiment to other experiments or theoretical calculations. Unfolding is used to determine this factor.
- $\mathcal{L}_{int}$  is the integrated luminosity during the period when the data was recorded.
- $A(p_T)$  is the geometrical detector acceptance.

- $\frac{dN^{jet}}{dp_T d\eta}$  is the inclusive jet momentum spectra.

Furthermore, it is useful to define the ratio of cross sections,

$$\mathcal{R}(p_T; R_1, R_2) = \frac{d^2\sigma(p_T; R_1)/d\eta dp_T}{d^2\sigma(p_T; R_2)/d\eta dp_T} \quad (5.2)$$

where  $\sigma(p_T; R_1)$  refers to the doubly differential cross section (Equation 5.3) of a jet with radius  $R_1$ . The ratio is carried out on a bin-by-bin basis per each  $p_T$  bin.

## 5.1 Raw Jet Spectra

This thesis reports inclusive jet results for radii between 0.1 and 0.5. Furthermore, jet results for radii  $R = 0.2$  and  $R = 0.4$  will be presented in the body of this chapter while results from the other radii will be limited to the appendix. Figure shows the raw (uncorrected)  $p_T$  spectra for inclusive jets from both MB and EMCAL triggered data. It is also evident from Figure that the EMCAL triggered data extends the  $p_T$  reach

## 5.2 8 TeV Data Quality

ALICE is a state-of-the-art experiment with excellent tracking and particle identification capabilities as discussed in Chapter 3. However, just like any real world experiment, it contains a number of inefficiencies and imperfections. This means that the data collected during the 8 TeV pp collision must be examined and any inaccuracies in the data must be removed before hard physics conclusions may be reached. Data may be compromised at both the event-level, the experiment erroneously recorded something as an event, or at the constituent-level, one of the subdetectors mismeasured a feature of a particle, and these outliers must be accounted for and removed

## 5.3 Event Selection

For an event to be selected into a physics analysis it must pass a number of quality control tests. For example, the LHC must have been in a state of stable beams, cosmic rays must be

excluded by only accepting tracks that originate from a vertex inside the detector, and the relevant detectors for a given analysis must be functioning as intended. Event selection and QA is implemented via a centralized class, `AliEventCuts`, within the `AliRoot` framework. This class contains a number of corrections including:

- 
- Another entry in the list

Further more the class `AliAnalysisTaskEmcalCorrection` within the `AliRoot` framework performs a number of corrections to the tower-level within physics analysis dependent on the EMCal. These corrections include:

- Energy calibration: Remove double counting due to the amount of energy typically deposited by a Hadron.
- Bad Channel Map: Remove both dead and hot towers from the EMCal clusterize based on an iterative average energy per occupancy algorithm
- Time Calibration: Remove slow particles, such as neutrons, which readout to the EMCal after the event has been recorded.
- Exotics Correction: Remove inefficiencies due to how a particle interacted with the EMCal.

After the above cuts are performed on EMCal towers the cells compromising the towers are clustered together using a clusterization algorithm

During the 8 TeV data collection period approximately 180 million minimum bias events were recorded, as summarized in table ?? . These events are separated into periods, which dictate the particular beam and detector configurations during the data taking. The 8 TeV data is broken into 7 periods with approximately 181 million minimum bias events recorded. This minimum bias sample corresponds to an integrated luminosity,  $\mathcal{L}_{int}$ , of  $8.95 pb^{-1}$  during this time period[47].

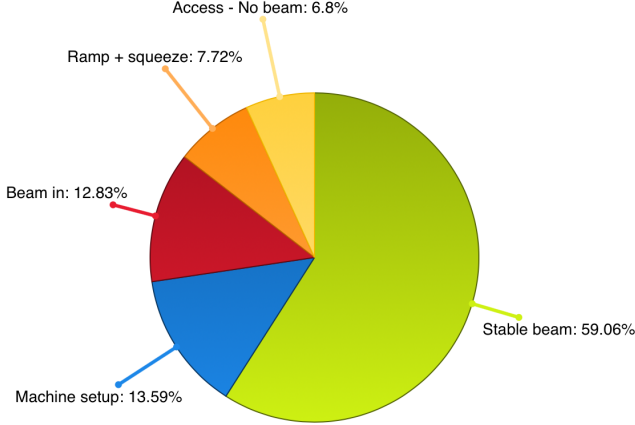


**Figure 5.1:** LHC state during the 8 TeV run.

Approximately, 15% of the data sampled is unusable due to malfunctions in TPC chambers, EMCAL super modules, the electronics for the EMCAL or TPC, and

## 5.4 Raw measurements

The ALICE experiment is capable of two types of jet reconstruction, charged and full jets. Charged jets use information from the charged particle tracking detectors, such as the ITS and TPC, in conjunction with a jet finding algorithm to identify jets. Full jets implement a similar procedure but also incorporates the EMCAL in order to

Period	# of runs	# of Min Bias events
LHC12c	89	$\sim 24$ M
LHC12d	140	$\sim 62$ M
LHC12e	5	$\sim 2$ M
LHC12f	56	$\sim 15$ M
LHC12g	8	$\sim 0.4$ M
LHC12h	159	$\sim 75$ M
LHC12i	40	$\sim 3$ M
Total	497	$\sim 181$ M

**Table 5.1:** 2012 8 TeV data taking period.

### 5.4.1 Raw Jet Momentum Spectra in pp Collisions

## 5.5 EMCAL Triggered Data

In addition with the minimum bias data collected, the EMCAL was used during the 8 TeV run in order to provided an enhanced data set that is preferential to hard processes. The Level-1 trigger[48] in the EMCAL has a associated trigger,  $\epsilon$ , of

$$\epsilon = \frac{N_{events}^{Triggered}}{N_{events}^{MinBias}} \times \frac{d^2 N_{Triggered}^{jet}}{d\eta dp_T} \Bigg/ \frac{d^2 N_{MinBias}^{jet}}{d\eta dp_T} \quad (5.3)$$

### 5.5.1 Acceptance Correction

Jet spectra, cross sections, and ratios of cross sections are reported over the full azimuth angle and psuedorapidity acceptance. However, due to jets being constrained to the EMCAL, a geometric factor is used to correct for the limited acceptance of the detector. This thesis uses a maximum jet radius of 0.5 to help study the effects of wide angle radiation on jet fragmentation. Heavy-ion use smaller jet radii, typically of 0.2, to help negate the high multiplicity background. Due to these geometric corrections the centroid of a jet is constrained to,

$$|\eta_{jet}| \leq 0.7 - R, \quad 1.4 + R \leq \phi_{jet} \leq 3.14 - R. \quad (5.4)$$

$$A(p_T) = \frac{(1.4 - 2R) \times (1.745 - 2R)}{2\pi}. \quad (5.5)$$

For jets between  $R = 0.1$  through  $R = 0.5$  the following jet acceptance corrections are used.

## 5.6 Unfolding

The reconstructed jet  $p_T$  has a number of detector effects ‘folded’ into the measurement. These effects included such things as:

- Tracking inefficiencies from the TPC and ITS.
- Missing jet energy components from long-lived particles, such as the  $K_L^0$  and neutron, that are cut by the EMCAL timing requirement.
- TPC track  $p_T$  and EMCAL cluster energy resolutions.
- Hadronic corrections to the EMCAL cluster spectrum.
- Material loss in the detectors.

Unfolding is the method by which these detector effects are removed from the raw inclusive jet spectra and a ‘true’ jet spectra may be obtained and compared with theoretical calculations or other experimental results. In order to unfold a jet spectra it is necessary to generate a response matrix that simulates the described effects above, after the response matrix is generated a number of statistical approaches including, Bayesian, Singular Value Decomposition (SVD), or Bin-by-Bin, may be applied to unfold the raw jet spectra. In order to generate the response matrix we embed a Pythia generated event into a GEANT3 simulation of the ALICE detector. Due to the fact that the performance and efficiency of the ALICE detector may change between the data taking periods each simulation is ‘anchored’ to a given LHC, these anchors contain all the hot and dead sectors for the subdetectors, along with their calibrated performance during that specified data taking. Two Monte Carlo data sets were produced with the MB trigger for the full 8 TeV run, the first was a Pythia generator using the Monash-2013 tune and the second was a MB tune of the PHOjet Monte Carlo package. Both data sets were explored for this thesis and it was decided that the final corrected spectra would be obtained via unfolding with the Pythia MC data set. The

Jet R	$A(p_T)$
0.1	0.296
0.2	0.214
0.3	0.146
0.4	0.091
0.5	0.048

**Table 5.2:** EMCAL jet acceptance for radii 0.1 - 0.5.

magnitude of any one of the effects unfolding is supposed to account for is not expected to be very large, but combined may be significant, thus unfolding is an important step in this analysis.

### 5.6.1 Response Matrix

Given a truth-level particle jet  $p_T$  we wish to reconstruct that jet's  $p_T$  at the detector-level. The particle-level pythia jets are constructed from the primary particles generated via Pythia while excluding any daughter decay particles in order to avoid double counting. In addition the tracking efficiency in Pythia is known to deviate from nature. This is due to Pythia under predicting the production of strange quarks. Constructing the response matrix in this case is calculated on a jet-by-jet basis. The particle-level jet centroid  $(\phi_{part}, \eta_{part})$  is matched to the detector-level jet via a constrain on the displaced distance between the two jet centroids in  $(\phi, \eta)$ . This distance was constrained to:  $\Delta R = \sqrt{(\phi_{part} - \phi_{det})^2 + (\eta_{part} - \eta_{det})^2} \leq 0.25$ . Once a jet is matched at the detector level to a jet generated from the particle level the response matrix is incremented by jet  $p_T$  at both the detector and Monte Carlo levels. The response matrix is generated with a fine binning with a width of 1 GeV per bin.

Figure 5.2 shows the response matrices for the  $R = 0.2$  (top left),  $R = 0.3$  (top right), and  $R = 0.4$  (bottom) jets generated with the prescribed manner. The response matrices display a linear relationship below 50 GeV on both axis and above 100 GeV the matrices are statistics starved. This is primarily due to the Monte Carlo Pythia and PhoJet data sets generated for the 8 TeV pp run did not model the high- $p_T$  triggers associated with the EMCAL. The particle jet finders configured for the response matrices allowed for jet finding down to a 100 MeV jet candidate at the particle level with no constraints on the minimum particle momentum or energy for a constituent. The detector level jet finders were configured in the same manner as the jet finders configured for the raw jet spectra measurement.

### 5.6.2 Corrections to Particle Level

Unfolding was performed using the `RooUnfold`[?] software package. Corrections are applied using the bin-by-bin[?] algorithm.

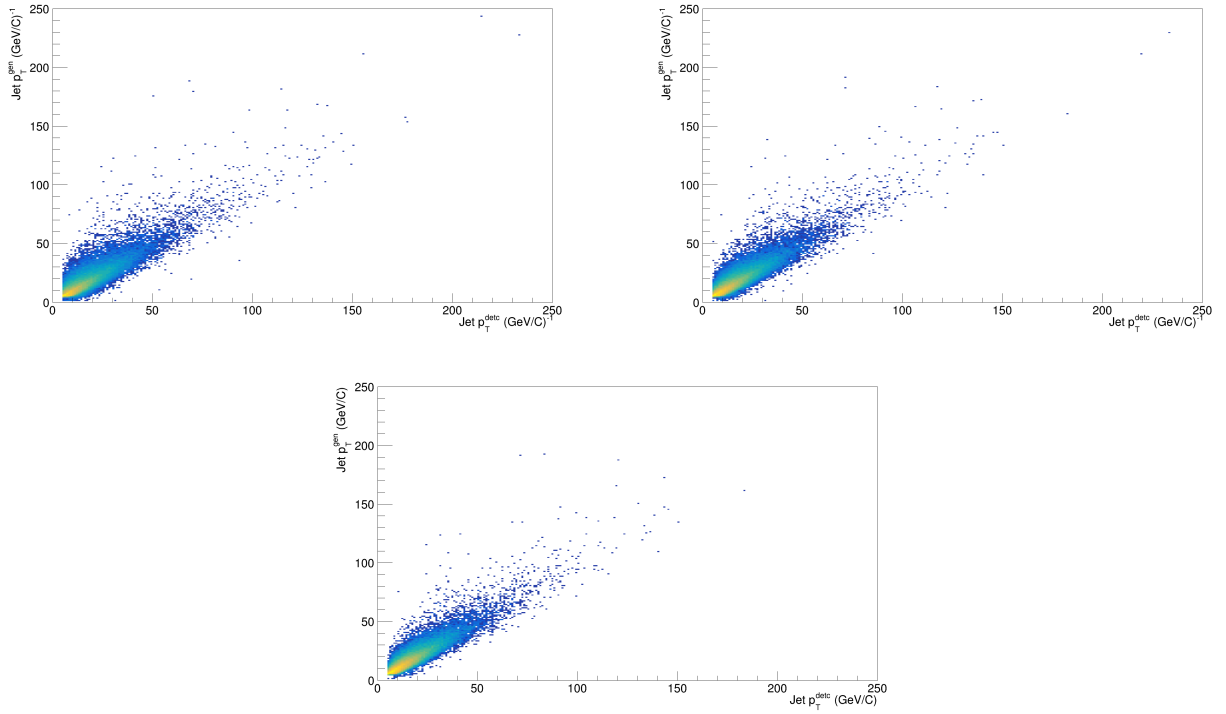


**Figure 5.2:** Response Matrices for  $R = 0.2$ ,  $R=0.3$ , and  $R = 0.4$  jets.

$$C_{MC}(p_T^{low} : p_T^{high}) = \frac{\int_{p_T^{low}}^{p_T^{high}} dp_T \frac{dF_{meas}^{uncorr}}{dp_T} \times \frac{d^2 N_{MC}^{particle}}{d\eta dp_T}}{\int_{p_T^{low}}^{p_T^{high}} dp_T \frac{dF_{meas}^{uncorr}}{dp_T}} \quad (5.6)$$

where  $d^2 N_{MC}^{particle}/dp_T d\eta$  is the PYTHIA level inclusive jet spectra,  $d^2 N_{MC}^{detector}/dp_T d\eta$  is the GEANT 3 level inclusive jet spectra,  $dF_{meas}^{uncorr}/dp_T$  is a weight function which minimizes the dependence on the two simulation spectra shapes, finally  $p_T^{low}$  and  $p_T^{high}$  are the lower and upper bin limits. Due to the limited statistics derived from the Monte Carlos available the unfolding procedure was stable only in unfolding the truth level jet spectra for the range:  $p_{T,jet} \in [10 \text{ GeV}, 120 \text{ GeV}]$  for both the raw Min Bias and Emcal triggered data sets. Due to the the final truth value for the jet spectra will be reported in this range.

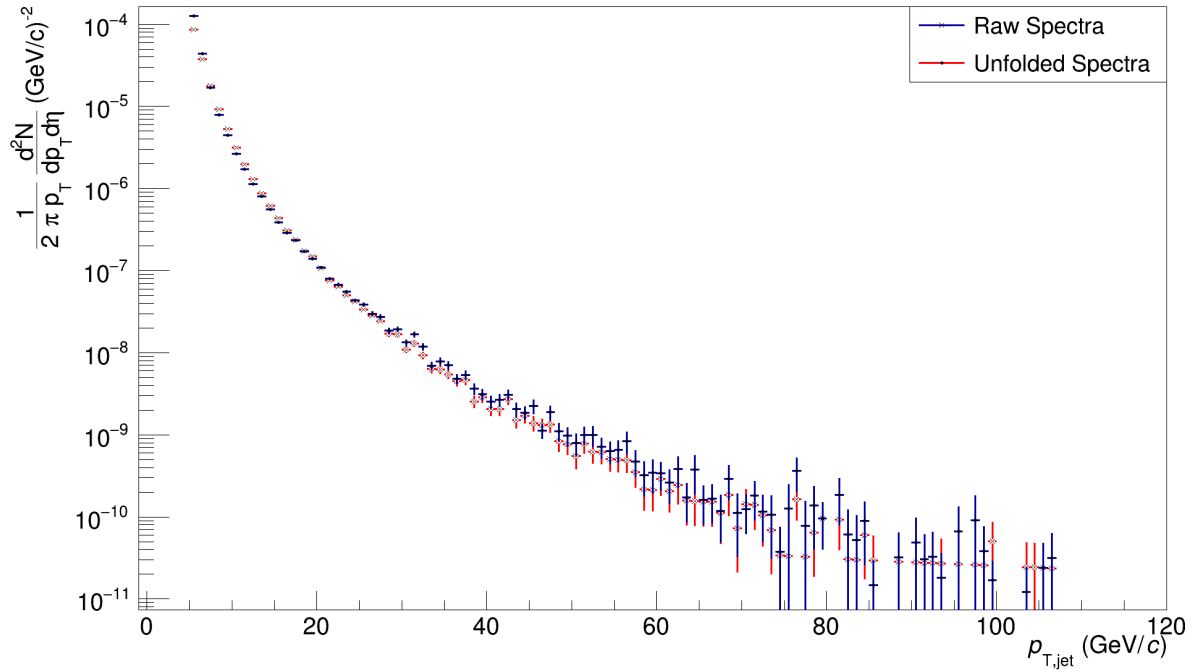


**Figure 5.3:** Unfolded jet spectra with fine binning for  $R = 0.3$

### 5.6.3 Unfolded MB Spectra

### 5.6.4 Unfolded EMCAL Triggered Spectra

## 5.7 Systematic Uncertainties

Systematic uncertainties arise due to our limited knowledge of the precise operating conditions and performance of the experiment and also due to any bias in our understanding of how to fundamental model the interactions. They systematics may therefore be broken into two components: uncertainties to the jet energy scale (JES) which shifts the momentum spectra along the x-axis and uncertainties in the jet yield which shift the spectra along the y-axis. The systematical and statistical uncertainties presented in this analysis will be presented as errors to the yield of the spectra. Due to the fact that the  $p_T$  distribution follows a power law function,  $dN/dp_T \sim p_T^{-5}$  uncertainties in the JES are converted to yield uncertainties by dividing each one by 5. Due to the low statistics at the highest  $p_T$  bins in this analysis, uncertainties in this regime my have large statistical fluctuations. Small ,systematic

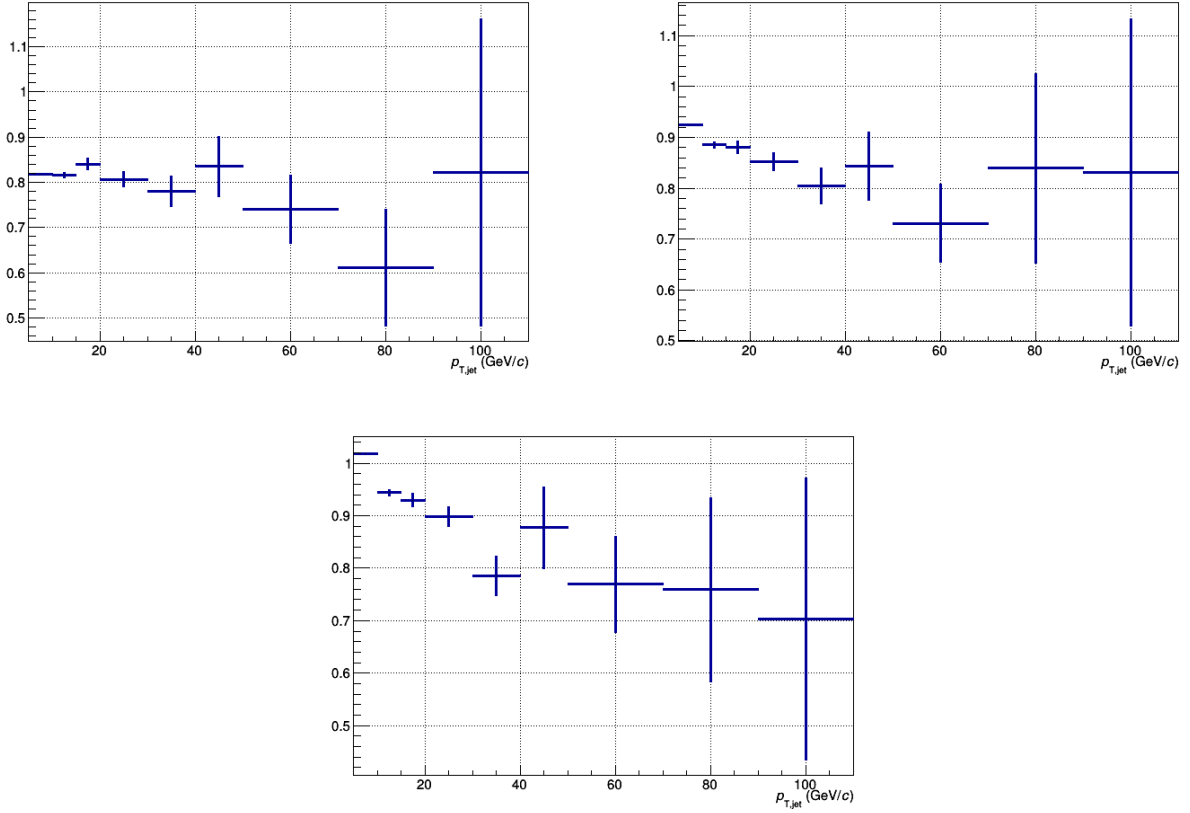


**Figure 5.4:** Systematic due to TPC tracking efficiency.

variations for the input of the jet spectra will have a dramatic effect over sparsely filled bins versus bins with a low granularity. As such it may be necessary to extrapolate the systematic from a low  $p_T$  bin to those at the highest  $p_T$  range. The systematics were performed on both the MB and EMCAL triggered data samples but no large variation was observed between the two, thus only the uncertainties from the MB sample are shown and are extrapolated to the triggered data.

### 5.7.1 Systematic Uncertainty to Jet Energy Scale

#### Tracking Efficiency

Corrections for the tracking efficiency were performed by randomly throwing out 5% of the tracks from each event from the 8 TeV data samples and reperforming jet on the altered data. All of the inputs for jet finding were maintained.

Figure 5.3 shows the systematical uncertainties for  $R = 0.2$  (top left),  $R = 0.3$  (top right), and  $R = 0.4$  (bottom) jets.

## Hadronic Correction

### EMCal Clusterization Algorithm

#### 5.7.2 Systematic Uncertainty to Jet Yield

##### Luminosity Uncertainty

The luminosity of a hadronic collider,  $\mathcal{L}$ , is given by the expression

$$\mathcal{L} = \frac{R}{\sigma} \quad (5.7)$$

where  $R$  is the interaction rate and  $\sigma$  is the visible cross section. Due to the fact that we only measure events within a 10 cm window within the primary vertex region we must scale the total luminosity to that which is delivered within the primary vertex region of the ALICE experiment. This scale factor is determined by dividing the total number of MB events to those accepted within the 10 cm window.  $N_{MB}^{tot}/N_{MB}^{10cmvertex} = 1.024$  from the acceptance criteria held in this analysis. The luminosity along with its uncertainty were determined during a special Van der Meer scan run in April of 2012[47]. The total systematic uncertainty for the minimum bias (MB) trigger were obtained by measuring the visible cross section using the T0 and V0 detectors. The MB trigger was defined as V0AND which required a hit in both the V0A and V0C. The cross section was reported as being a combined average for MB with the V0AND as,

$$\sigma_{V0} = (55.8 \pm 1.2)mb \quad (5.8)$$

with a combined systematic uncertainty of 2.19% on the visible cross section and 2.60% on the luminosity.

### 5.7.3 Total Uncertainty

A summary of the total systematic errors used in the final analysis.

Systematic	Systematic Errors		
	R = 0.2 Jets	R = 0.3 Jets	R = 0.4 Jets
Sensitivity to Clusterization	AF	AFG	004
Hadronic Correction	AX	ALA	248
Tracking Efficiency	AL	ALB	008
Sensitivity to Unfolding	DZ	DZA	012
Momentum Resolution	AS	ASM	016
Energy Resolution	AND	020	02
Angola	AO	AGO	024

The systematics from the yield and JES are added in quadrature together and this is combined in quadrature with the statistical errors.

## 5.8 Corrected pp jet cross section

### 5.8.1 Comparisons to pQCD predictions

### 5.8.2 Jet Cross Sections and Ratios

# Chapter 6

## Conclusion and Outlook

### 6.1 8 TeV Inclusive Jet Results from CMS and ATLAS

CMS[49] and ATLAS[50] both reported the double differential cross section for inclusive jets at 8 TeV.

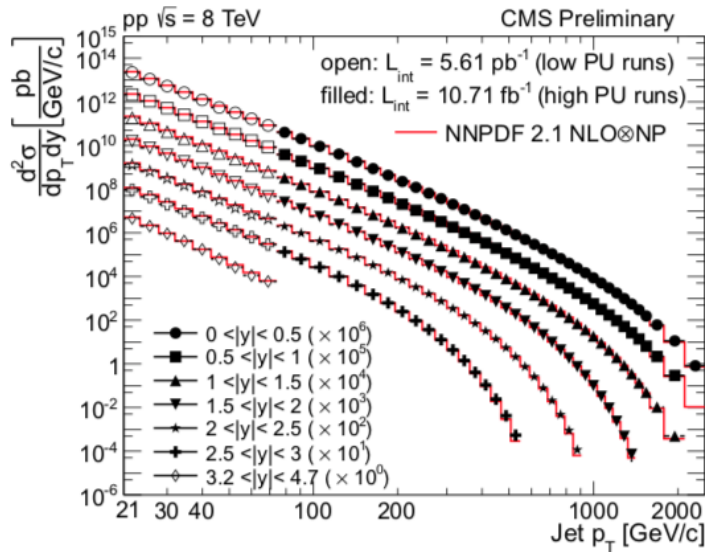


**Figure 6.1:** 8 TeV CMS inclusive jet cross sections with radii of  $R = 0.7$  and binned by jet rapidity compared to NLO calculations with non-perturbative corrections[49].

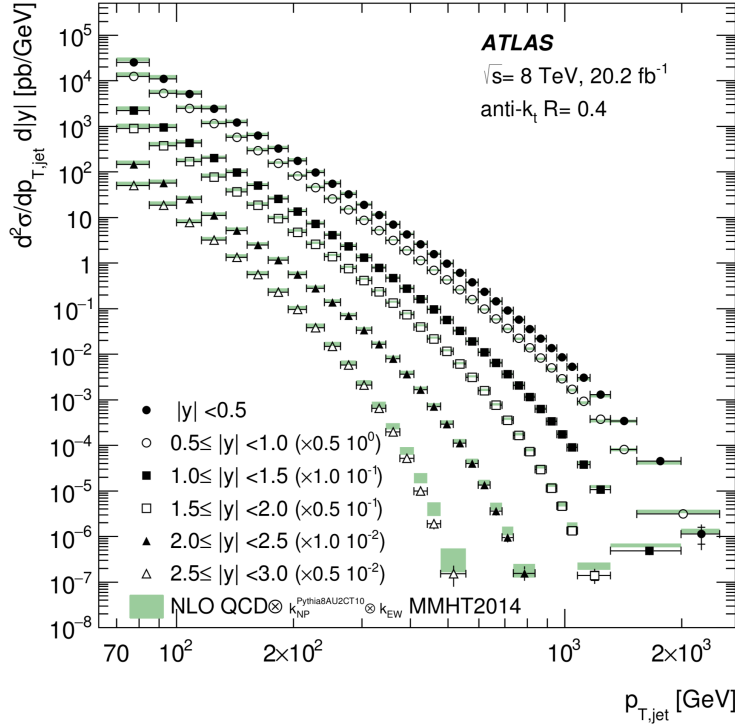


**Figure 6.2:**  $R = 0.4$  inclusive jet cross section at 8 TeV from ATLAS in binned by jet rapidity compared to NLO QCD predictions[50].

## 6.2 Inclusive Jet Spectra and Cross Section Ratios at 2.76 TeV

Inclusive jet spectra and cross section ratios were measured in the ALICE experiment using a 2011 pp 2.76 TeV data sample[46]. Jets were reconstructed using TPC tracks and EMCal clusters with the FastJet Anti- $K_T$  algorithm. Tracks with a minimum  $p_T \geq 150$  MeV and constrained to within 10 cm of the primary vertex were accepted into the jet finder. EMCal clusters were

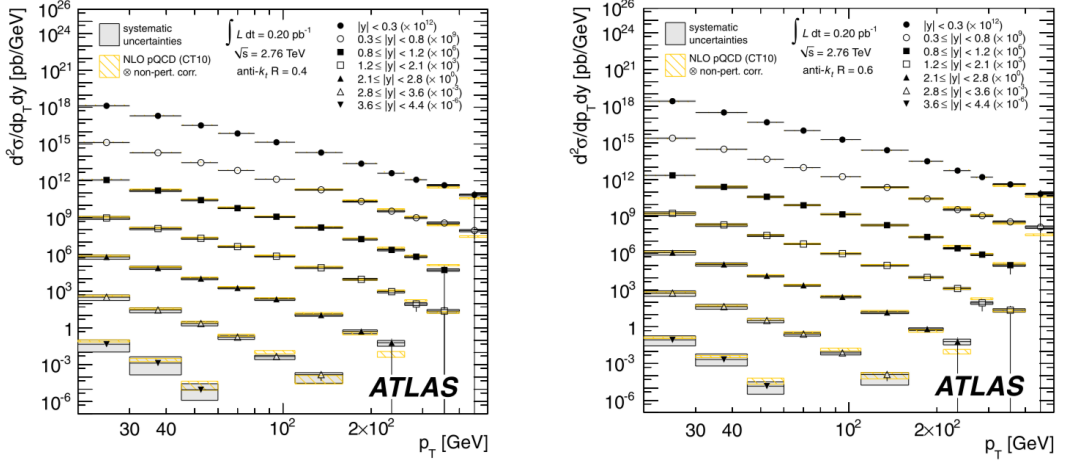


**Figure 6.3:** The 8 TeV ATLAS jet cross sections rescaled to better show comparisons with NLO and non-perturbative calculations at low  $p_T$ [50].

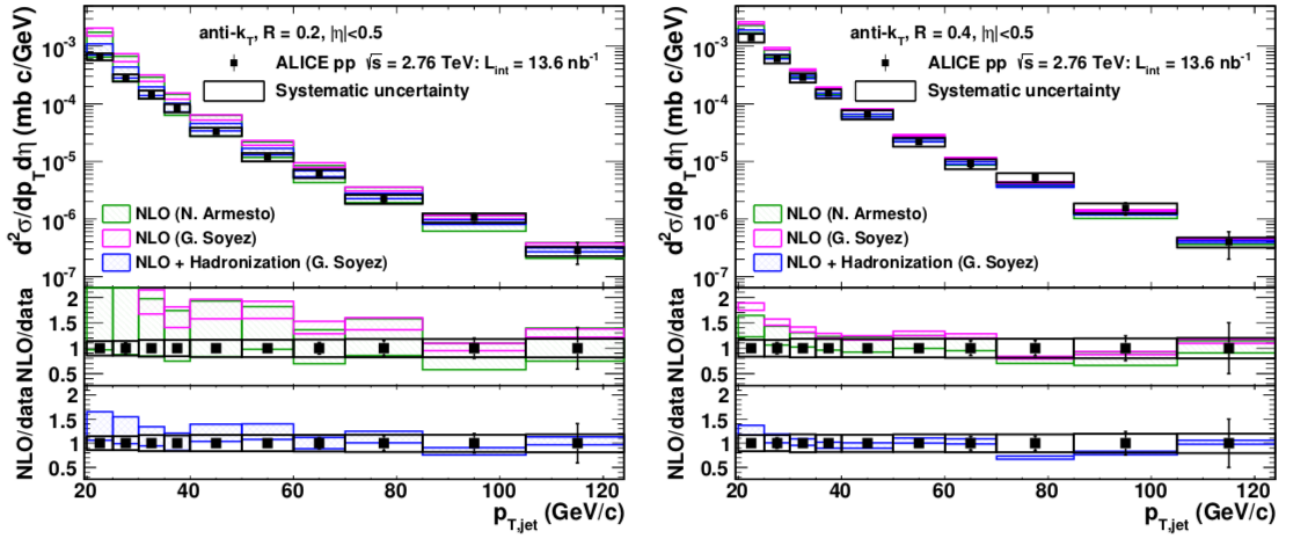


**Figure 6.4:** Inclusive differential cross section from the 2.76 TeV proton proton run with ALICE

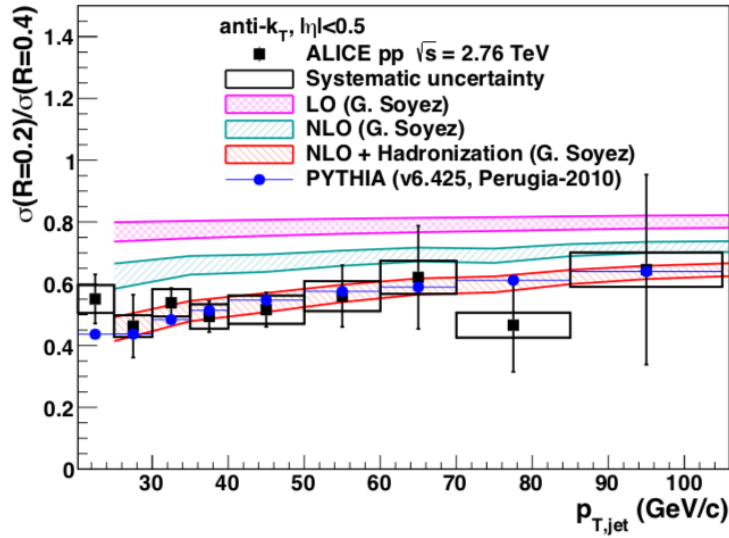


**Figure 6.5:** LHC state during the 8 TeV run.

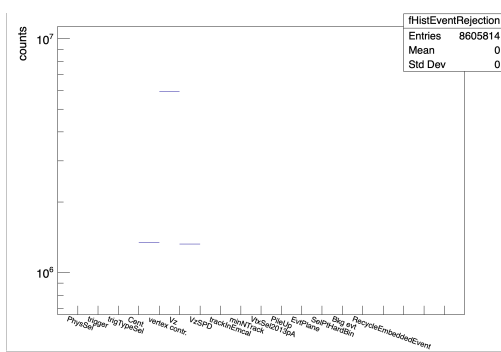


**Figure 6.6:** Minimum Bias Event Rejection

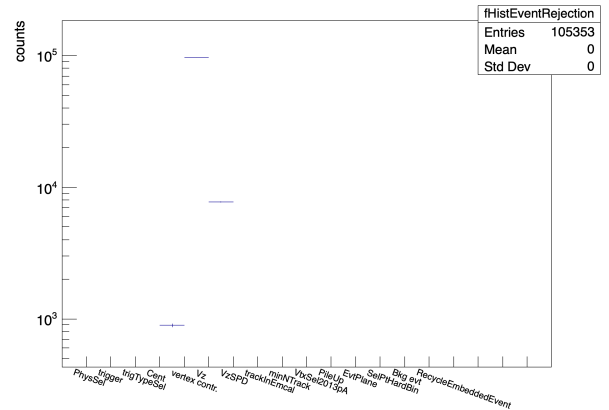


**Figure 6.7:** Emcal Triggered Event Rejection

# Bibliography

- [1] Michael Riordan. The discovery of quarks. *Science*, 256(5061):1287–1293, 1992. [4](#)
- [2] Frank Wilczek. Asymptotic freedom: From paradox to paradigm. *Proc. Nat. Acad. Sci.*, 102:8403–8413, 2005. [Rev. Mod. Phys.77,857(2005)]. [5](#)
- [3] Vardan Khachatryan et al. Measurement of the inclusive 3-jet production differential cross section in proton–proton collisions at 7 TeV and determination of the strong coupling constant in the TeV range. *Eur. Phys. J.*, C75(5):186, 2015. [5](#)
- [4] Jets at cms and the determination of their energy scale, July 2012. [6](#)
- [5] J. D. Bjorken. Asymptotic sum rules at infinite momentum. *Phys. Rev.*, 179:1547–1553, Mar 1969. [6](#)
- [6] J. D. Bjorken. Can We Measure Parton Parton Cross-Sections? *Phys. Rev.*, D8:4098, 1973. [6](#)
- [7] Matt Dobbs and Jorgen Beck Hansen. The HepMC C++ Monte Carlo event record for High Energy Physics. *Comput. Phys. Commun.*, 134:41–46, 2001. [8](#)
- [8] Wolfgang Kurt Hermann Panofsky. Low q electrodynamics, elastic and inelastic electron (and muon ) scattering. 1968. [9](#)
- [9] J. Feltesse. Introduction to Parton Distribution Functions. *Scholarpedia*, 5(11):10160, 2010. revision #186761. [9](#)
- [10] K. Kovarik, T. Jezo, A. Kusina, F. I. Olness, I. Schienbein, T. Stavreva, and J. Y. Yu. CTEQ nuclear parton distribution functions. *PoS*, DIS2013:274, 2013. [9](#)
- [11] Richard D. Ball, Valerio Bertone, Stefano Carrazza, Christopher S. Deans, Luigi Del Debbio, Stefano Forte, Alberto Guffanti, Nathan P. Hartland, José I. Latorre, Juan Rojo, and Maria Ubiali. Parton distributions for the LHC Run II. *JHEP*, 04(arXiv:1410.8849. EDINBURGH 2014-15. IFUM-1034-FT. CERN-PH-TH-2013-253. OUTP-14-11P. CAVENDISH-HEP-14-11):040. 138 p, Oct 2014. Comments: 138 pages, 64 figures. Several typos in text and references corrected, one reference added). [9](#)

- [12] Harald Fritzsch. QCD: 20 years later. In *QCD 20 Years Later: Proceedings, Workshop, Aachen, Germany, June 9-13, 1992*, pages 827–852, 1992. [10](#)
- [13] John C. Collins, Davison E. Soper, and George F. Sterman. Factorization of Hard Processes in QCD. *Adv. Ser. Direct. High Energy Phys.*, 5:1–91, 1989. [10](#)
- [14] Nora Brambilla, Xavier Garcia i Tormo, Joan Soto, and Antonio Vairo. The Logarithmic contribution to the QCD static energy at  $N^{**}4$  LO. *Phys. Lett.*, B647:185–193, 2007. [10](#)
- [15] Martin Erdmann. Investigation of quark - anti-quark interaction properties using leading particle measurements in  $e^+ e^-$  annihilation. *Phys. Lett.*, B510:29–35, 2001. [10](#)
- [16] B. R. Webber. Hadronization. In *Proceedings: Summer School on Hadronic Aspects of Collider Physics, Zuoz, Switzerland, Aug 23-31, 1994*, pages 49–77, 1994. [11](#)
- [17] Bo Andersson, Sandipan Mohanty, and Fredrik Soderberg. Recent developments in the Lund model. In *36th Annual Winter School on Nuclear and Particle Physics (PINP 2002) and 8th St. Petersburg School on Theoretical Physics St. Petersburg, Russia, February 25-March 3, 2002*, 2002. [12](#)
- [18] B. R. Webber. A QCD Model for Jet Fragmentation Including Soft Gluon Interference. *Nucl. Phys.*, B238:492–528, 1984. [12](#)
- [19] L. L. Jenkovszky, V. K. Magas, J. T. Londergan, and A. P. Szczepaniak. Explicit Model Realizing Parton-Hadron Duality. *Int. J. Mod. Phys.*, A27:1250157, 2012. [13](#)
- [20] Jan Rak and Michael J. Tannenbaum. *QCD in hard scattering*, pages 214–243. Cambridge Monographs on Particle Physics, Nuclear Physics and Cosmology. Cambridge University Press, 2013. [13](#)
- [21] Ryan Atkin. Review of jet reconstruction algorithms. *J. Phys. Conf. Ser.*, 645(1):012008, 2015. [14](#), [17](#)

- [22] J E Huth, N Wainer, K Meier, N J Hadley, F Aversa, Mario Greco, P Chiappetta, J P Guillet, S Ellis, Zoltán Kunszt, and Davison Eugene Soper. Toward a standardization of jet definitions. (FERMILAB-CONF-90-249-E):7 p, Dec 1990. [14](#)
- [23] Gerald C. Blazey et al. Run II jet physics. In *QCD and weak boson physics in Run II. Proceedings, Batavia, USA, March 4-6, June 3-4, November 4-6, 1999*, pages 47–77, 2000. [14](#)
- [24] Matteo Cacciari, Gavin P. Salam, and Gregory Soyez. FastJet User Manual. *Eur. Phys. J.*, C72:1896, 2012. [18](#)
- [25] Megan Connors, Christine Natrass, Rosi Reed, and Sevil Salur. Jet measurements in heavy ion physics. *Rev. Mod. Phys.*, 90:025005, 2018. [19](#)
- [26] R Brun, F Bruyant, M Maire, A C McPherson, and P Zanarini. *GEANT 3: user's guide Geant 3.10, Geant 3.11; rev. version*. CERN, Geneva, 1987. [19](#)
- [27] Torbjorn Sjostrand, Stephen Mrenna, and Peter Z. Skands. A Brief Introduction to PYTHIA 8.1. *Comput. Phys. Commun.*, 178:852–867, 2008. [19](#)
- [28] Peter Zeiler Skands. Tuning Monte Carlo Generators: The Perugia Tunes. *Phys. Rev.*, D82:074018, 2010. [20](#)
- [29] A. Capella, U. Sukhatme, C.-I. Tan, and J. Tran Thanh Van. Dual parton model. *Physics Reports*, 236(4):225 – 329, 1994. [20](#)
- [30] Cheuk-Yin Wong. *Introduction to high-energy heavy-ion collisions*. World Scientific, Singapore, 1994. Erratum. [20](#)
- [31] Fritz W. Bopp, R. Engel, and J. Ranft. Rapidity gaps and the PHOJET Monte Carlo. In *High energy physics. Proceedings, LAFEX International School, Session C, Workshop on Diffractive Physics, LISHEP'98, Rio de Janeiro, Brazil, February 16-20, 1998*, pages 729–741, 1998. [20](#)
- [32] Bedangadas Mohanty. Exploring the QCD phase diagram through high energy nuclear collisions: An overview. *PoS*, CPOD2013:001, 2013. [21](#), [24](#)

- [33] T. Csorgo. New form of matter at CERN SPS: Quark matter but not quark gluon plasma. *Nucl. Phys. Proc. Suppl.*, 92:62–74, 2001. [,62(2000)]. [21](#)
- [34] I. Arsene et al. Quark gluon plasma and color glass condensate at RHIC? The Perspective from the BRAHMS experiment. *Nucl. Phys.*, A757:1–27, 2005. [21](#)
- [35] K. Adcox et al. Formation of dense partonic matter in relativistic nucleus–nucleus collisions at rhic: Experimental evaluation by the {PHENIX} collaboration. *Nuclear Physics A*, 757(1–2):184 – 283, 2005. First Three Years of Operation of {RHIC}. [21](#)
- [36] B.B. Back et al. The {PHOBOS} perspective on discoveries at {RHIC}. *Nuclear Physics A*, 757(1–2):28 – 101, 2005. First Three Years of Operation of {RHIC}. [21](#)
- [37] J. Adams et al. Experimental and theoretical challenges in the search for the quark–gluon plasma: The {STAR} collaboration’s critical assessment of the evidence from {RHIC} collisions. *Nuclear Physics A*, 757(1–2):102 – 183, 2005. First Three Years of Operation of {RHIC}. [21](#)
- [38] Barbara V. Jacak and Berndt Müller. The exploration of hot nuclear matter. *Science*, 337(6092):310–314, 2012. [21](#)
- [39] J. D. Bjorken. Highly relativistic nucleus-nucleus collisions: The central rapidity region. *Phys. Rev. D*, 27:140–151, Jan 1983. [23](#)
- [40] Shanshan Cao, Tan Luo, Guang-You Qin, and Xin-Nian Wang. Heavy and light flavor jet quenching at rhic and lhc energies. *Physics Letters B*, 777:255 – 259, 2018. [22](#)
- [41] Michael L. Miller, Klaus Reygers, Stephen J. Sanders, and Peter Steinberg. Glauber modeling in high energy nuclear collisions. *Ann. Rev. Nucl. Part. Sci.*, 57:205–243, 2007. [23](#)
- [42] Morad Aaboud et al. Measurement of the nuclear modification factor for inclusive jets in Pb+Pb collisions at  $\sqrt{s_{\text{NN}}} = 5.02$  TeV with the ATLAS detector. *Phys. Lett.*, B790:108–128, 2019. [23](#), [24](#)

- [43] Klochkov and I Selyuzhenkov and. Centrality determination in heavy-ion collisions with the CBM experiment. *Journal of Physics: Conference Series*, 798:012059, jan 2017. [23](#)
- [44] James L. Nagle and William A. Zajc. Small System Collectivity in Relativistic Hadronic and Nuclear Collisions. *Ann. Rev. Nucl. Part. Sci.*, 68:211–235, 2018. [25](#)
- [45] Wenbin Zhao, You Zhou, Hao jie Xu, Weitian Deng, and Huichao Song. Hydrodynamic collectivity in proton–proton collisions at 13 tev. *Physics Letters B*, 780:495 – 500, 2018. [25](#)
- [46] Rongrong Ma. Measurements of the inclusive jet cross section and jet fragmentation in pp collisions with the alice experiment at the lhc. *Nuclear Physics A*, 910-911:319 – 322, 2013. Hard Probes 2012. [65](#)
- [47] ALICE luminosity determination for pp collisions at  $\sqrt{s} = 8$  TeV. Mar 2017. [55](#), [62](#)
- [48] O. Bourrion, R. Guernane, B. Boyer, J. L. Bouly, and G. Marcotte. Level-1 jet trigger hardware for the ALICE electromagnetic calorimeter at LHC. *JINST*, 5:C12048, 2010. [57](#)
- [49] CMS Collaboration. Measurement of the double-differential inclusive jet cross section at  $\text{sqrt}(s) = 8$  TeV with the CMS detector. 2013. [64](#)
- [50] Morad Aaboud et al. Measurement of the inclusive jet cross-sections in proton-proton collisions at  $\sqrt{s} = 8$  TeV with the ATLAS detector. *JHEP*, 09:020, 2017. [64](#), [65](#), [66](#)

# Appendices

# Vita